IPP-Report

Max-Planck-Institut für Plasmaphysik

Vassily Burwitz

Temperature Programmed Desorption of Helium in Tungsten

IPP 2017-11
Dezember 2017

Technische Universität München
Fakultät für Physik

Abschlussarbeit im Masterstudiengang Physik

Temperatur-induzierte Desorptionsmessungen von Helium in Wolfram

Temperature Programmed Desorption of Helium in Tungsten

Vassily Burwitz

4. Oktober 2017

Max-Planck-Institut für Plasmaphysik

Erstgutachter (Themensteller): Prof. R. Neu
Zweitgutachter: Prof. P. Feulner

Contents

1 Introduction **1**

2 Fundamentals **3**
2.1 Helium in Nuclear Fusion Research . . . 3
2.2 Important Physical Concepts for the Helium-in-Tungsten System . . 4
2.2.1 Diffusion in Metallic Solids . . . 4
2.2.1.1 Jump-diffusion Model . . . 4
2.2.1.2 Trapping Sites . . . 5
2.2.2 Helium in Tungsten . . . 6
2.3 Temperature Programmed Desorption . . . 7
2.3.1 Theory of TPD . . . 7
2.3.2 Time- to Temperature-dependence Conversion . . . 9
2.4 Rate-Equation Modelling . . . 10
2.4.1 Working Principle . . . 10
2.4.2 TESSIM-X . . . 10
2.5 Ion Beam Analysis . . . 11
2.5.1 Theory . . . 11
2.5.2 Elastic Recoil Detection Analysis . . . 12
2.5.3 Nuclear Reaction Analysis . . . 13
2.6 Sample Preparation . . . 14

3 Design and Commissioning of the High Temperature TPD Setup **17**
3.1 The TESS Setup . . . 17
3.2 Determining the Design Criteria . . . 18
3.2.1 Absolute Quantifiable Measurements . . . 18
3.2.2 Accurate Temperature Measurement over the Full Ramp . . . 18
3.2.3 Minimal 4 $\frac{amu}{q}$ Channel Background . . . 18
3.2.4 High Sample Processing Rate . . . 19
3.2.5 Maximum Temperature $> 2700\,\mathrm{K}$ . . . 19
3.2.6 Sample Heating Rates in $5\,\mathrm{K/s} \geq R_{heating} \geq 0.05\,\mathrm{K/s}$ Range . 20
3.3 Upgrading TESS . . . 21
3.3.1 Working Principle of an Electron Beam Heater . . . 21
3.3.2 Mechanical Structure . . . 22
3.3.3 Temperature Measurement . . . 25

3.3.4 Heating Unit 27
3.3.5 Vacuum System 28
3.3.6 Mass Spectrometry Measurement 30

4 Results and Discussion **33**
4.1 Modelling 33
4.2 ERDA Results 39
4.2.1 Energy Calibration 39
4.2.2 Absolute Quantification 40
4.2.3 Measurement of He-implanted W 41
4.3 TPD Results 45
4.4 Notes on the Usage of the TPD Setup 47
4.5 Discussion of Experimental Results 50
4.5.1 Desorption Peaks 50
4.5.2 He Migration Dynamics 55
4.6 Comparison of Measurement and Simulation 58

5 Conclusion and Outlook **61**

A Calculations **63**
A.1 Relation for the Power Output of an Electron Beam Heater 63
A.2 Pyrometer Reference Measurement 65
A.3 Depth Resolution of ERDA 67
A.4 Evaporation Rates 68

B Tables **69**

Bibliography **75**

Chapter 1

Introduction

Helium implanted into tungsten is of great interest both from a purely scientific and from an engineering point of view.

On the scientific side, the behavior of helium (He) implanted into tungsten (W) is of great interest as it displays a distinctly unexpected behavior. Although He is a noble gas and hence is not expected to form interatomic bonds, it - when trapped in tungsten - seems to attract other He atoms. In fact these agglomerations can grow from a single atom to macroscopic bubbles [1]. Another interesting feature is the growth of so called "fuzz" when W is subject to a high flux He plasma or ion beam for prolonged periods of time while being held at high temperatures. These coral-like structures on the µm scale can retain more than 10 atomic% He [2, 3].

Nuclear engineers are interested in the system because it is planned to use tungsten as inner wall material in a future magnetic confinement nuclear fusion reactor. In such a reactor there will be multiple sources of He. For the design process it is therefore essential to predict the evolution of tungsten components exposed to He.

A common method to study gaseous inclusions in metals is Temperature Programmed Desorption (TPD). It is a well established experimental technique, that measures the desorption of gases from a solid as function of temperature. Therefrom both the binding energy of the gas atoms in the solid and the total amount of gas desorbed from the solid can be calculated. Beginning with its inception it has been used to study adsorbates on tungsten [4]. The first study using TPD on the He-in-W system was carried out in 1965 [5], with a series of in-depth studies following in the 1970s [6, 7] using ions with implantation energies up to 5 keV [8]. The studies showed that it requires very high temperatures ($> 2000\,\mathrm{K}$) to completely remove He once it has been implanted into W. However, although there have been many experimental and computational studies undertaken since then, there is still a lack of understanding of the exact dynamics of He transport and retention in W. As part of this work the current knowledge base will be used as input for a rate equation program and the results compared with experimental TPD data.

The main goal of this thesis was to design and commission a TPD setup that is capable of conducting He TPD studies. This is a challenging task due to the high temperatures and good vacuum required. The new setup was integrated into the Thermal

Effusion Spectroscopy Setup (TESS), the Max-Planck-Institut für Plasmaphysik's (IPP) material science divisions workhorse for TPD studies. The accuracy of the setup was confirmed by independently determining the He content of a reference sample with Elastic Recoil Detection Analysis (ERDA) prior to TPD. ERDA is an ion beam analysis technique well suited to detect light atoms (e.g. He) in a matrix of heavy atoms (e.g. W) [9]. The measurements were conducted using an existing ERDA setup on the RKS beamline of the tandem accelerator facility at IPP.

With the reference measurements it was proven that all He implanted can indeed be detected by the TPD setup. This demonstrated the unique capabilities of the new setup.

Chapter 2

Fundamentals

In this chapter a description of the He-in-W system is given. Furthermore, the experimental and computational techniques employed to characterize it are described.

2.1 Helium in Nuclear Fusion Research

Understanding the interaction of He with metals is an important step on the way towards a future nuclear fusion power plant. It is currently foreseen that the first reactor to have a positive net power output will use the $D(^3T,^1n)^4He$ reaction as energy source. This first prototype power plant will be outfitted with a divertor made of W [10]. The divertor will be subject to a high flux of neutrals and ions from the fusion plasma. It will also have to withstand high energy loads. At the same time it will be subjected to 14 MeV neutron bombardment.

When examining the nuclear fusion reactor environment in detail, there are a total of three sources of He. Firstly, the power generating reaction has ^{4}He as one of its products. The He is created in the plasma and impinges on the reactor vessel walls as an ion or neutral at eV energies and fluxes of the order of $10^{22\pm1}\ \frac{\mathrm{He}}{m^2\ \mathrm{s}}$ [2, 11]. Its concentration is predicted to reach approx. 1 at.% in the divertor surface [12]. The second source is ^{3}He from tritium decay. As hydrogen isotopes can diffuse deep into metals, this will act as a He source in the bulk. The energy imparted on the ^{3}He in the $^3_1\mathrm{H}\rightarrow^3_2\mathrm{He}+e^-$ is negligibly small. The ^{3}He is expected to accumulate to concentrations of around tens to hundreds of appm [13]. A third source are α-particles produced in the bulk by the decay of radioactive elements that are created by transmutations induced by the fusion neutrons. The α-particles will initially have energies in the MeV range. This will make them cause additional displacement damage to the lattice structure of the host metal. This source of He is predicted to accumulate to approx. 1 appm [13].

The following is known about the effects of He on the macroscopic properties of W: He leads to surface hardening [14]. He creates bubbles that grow - if a sufficient amount of He is provided - until they form surface blisters that eventually burst; or, if there are many bubbles in a layer, the sample surface delaminates [1, 15]. At higher implantation temperatures a coral-like micro structure called "fuzz" grows

that can hold more than 10 at.% He [2, 3]. The dynamics of this process are not quantitatively understood. Qualitatively it is known that thresholds for blistering and fuzz growth depend on the He implantation conditions. Important factors are temperature, fluence, energy and flux. A microscopic understanding of the role He plays in the described phenomena is, however, lacking.

2.2 Important Physical Concepts for the Helium-in-Tungsten System

First, some of the dynamics ongoing in a crystal containing impurities are explained, then the dynamics of He in W are described.

2.2.1 Diffusion in Metallic Solids

Diffusion in metallic solids is described by the phenomenological Fick's law [16]:

$$\boldsymbol{J} = -D\ \nabla n \tag{2.1}$$

In this equation $\boldsymbol{J}$ is the particle flux density, i.e., the number of particles passing though a unit area in unit time. D is the diffusion coefficient, a temperature- and material-dependent parameter. Lastly, n is the number density of the diffusing species. Diffusive transport occurs from regions of high to regions of low concentration; therefore, there is a minus sign in front of the gradient.

The diffusion ongoing in a metallic crystalline solid can be categorized into three different types: Self diffusion, interdiffusion and impurity diffusion.

Self-diffusion describes the process of atoms of the same species interchanging position. Interdiffusion is the diffusive mixing of different species at an interface. Lastly, impurity diffusion is the diffusive introduction and migration of small (trace) quantities of impurity atoms that do not form part of the lattice. In this process the trace atoms distribute themselves homogeneously within the metal given a sufficient amount of time and periodic boundary conditions. The diffusion of He in W falls into the latter category.

2.2.1.1 Jump-diffusion Model

In the literature the jump-diffusion model is also called diffusion-trapping model or diffusion-reaction model. In the model, atoms are considered to "jump" from one potential well to the next. In the classical picture they can only perform a "jump" when they have a kinetic energy larger than the potential energy step of the well. Quantum mechanical tunneling is not considered. The atoms are assumed to be

oscillating inside the well and attempt to "escape" every time they encounter its edge. This oscillation frequency is called attempt frequency (ν_a).

Often a theoretical value, the Debye frequency, is used for the attempt frequency, although measured values have been found to deviate from this value by more than one order of magnitude [17, 18]. It will be explained in section 2.3.1 how ν_a can be determined experimentally.

As trace atoms thermalize within the lattice their energy distribution can be described by the temperature (T) of the solid. This gives a probability of $e^{-\frac{E}{k_B T}}$ for an atom to escape from a potential well of depth (E) if the crystal lattice is at temperature (T).

2.2.1.2 Trapping Sites

Any geometrical configuration in the structure of a solid that shapes the potential energy surface in such a manner that it forms a potential well can act as a trapping site. There are intrinsic trapping sites defined by the undisturbed potential energy surface of the crystal structure, and there are extrinsic sites that only exist if the crystal lattice is imperfect.

Intrinsic trapping sites are local minima defined by the electron cloud topography of the lattice and trace atom. The general term used for these sites is either lattice site or solute site. The position of these sites is usually determined by energy minimization calculations using density-functional-theory-based codes. They depend on the lattice type and are named according to the shape of the volume spanned by the nearest neighbor atoms in the crystal lattice, e.g., "tetrahedral site". The energy barriers of these sites are usually low in comparison to sites induced by defects.

Extrinsic trapping sites are due to deviations from the perfect lattice structure. Two common types are vacancies (empty lattice positions) and interstitials (additional atoms of the lattice species that are not in a regular lattice position). Another are impurities, i.e., atoms not belonging to the lattice species but in lattice positions. Further defect types include different irregularities in the lattice layer configuration. The crystal surface and grain boundaries are also - due to the discontinuity of the lattice there - zones with possible trapping sites. Crystal defects are always present in a material. Their lower limit is defined by $n \approx \mathrm{e}^{-\frac{c_1 E}{k_B T}}$ where c_1 depends on the defect type and E is the energy required to create the defect [19]. In a real crystal the defect density is larger than this theoretical lower limit. Albeit, it is possible to decrease the number of defects by holding a sample at high temperatures for a sufficient amount of time. This process is called annealing. For example, after heating a tungsten crystal to 2000 K for 2 min, the residual defect density is $< 10^{-5}$

defects per W atom; this value is deduced from deuterium retention measurements obtained by loading W with a low-temperature plasma while holding the samples at low temperature [17].

Trapping sites consisting of multiple vacancies, interstitials or combinations of these are referred to as clusters.

Irregularities in a crystal lattice can be created by particle bombardment, where the energy transferred to the lattice atom in a collision with the projectile or another target atom is larger then the displacement energy of the lattice. Another source is the mechanical deformation of a sample.

Self-trapping is the process in which an already trapped trace atom traps another atom of the same species at the same trapping site. If at a trapping site an agglomeration of trace atoms is formed by multiple iterations of this process, one speaks of cluster nucleation.

2.2.2 Helium in Tungsten

Due to its closed electron shell, He has a high heat of solution (E_{sol}) in tungsten. This makes He essentially insoluble in the crystal. Theoretical calculations yield a heat of solution of 5.47 eV [20], while experimental results suggest a value between 3 eV and 5 eV [1]. Once inside the lattice, He will diffuse rapidly; its migration energy being $E_m < 0.24$ eV [18, 21]. The insolubility in combination with the low migration energy make He either quickly leave the sample or precipitate at lattice defects. Once trapped at one of these defects, the required detrapping energy is high; depending on the defect type, it can be higher than 4.5 eV [18, 21]. Not only can single He atoms trap in empty defects, but it is also possible for multiple He atoms to self-trap at the same defect. The self-trapping process has been studied computationally [22]. Hereby, He trapping at vacancies was simulated. These recent results suggest that above a certain number of He atoms trapped per vacancy (≈ 3) the He detrapping energy does not decrease below a threshold no matter how many He atoms are trapped. The same study suggests, that above a certain number of He atoms trapped per vacancy ($7 - 15$), the energy required for detrapping a He atom becomes larger than the energy it costs to remove a W atom from its lattice site by creating a vacancy and an interstitial [22, 23]. This process is termed trap mutation. The combination of self-trapping and trap mutation makes it possible that from a single vacancy with a trapped He atom a macroscopic bubble can grow. Computational predictions are confirmed by the experimental observation of the formation of macroscopic bubbles during exposure with He ions even at energies below the lattice displacement energy, where the ions kinetic energy is ruled out as a source of damage, as long as a sufficiently large amount of He is provided [1, 24]. In this energy range displacement damage does not occur, therefore the bubbles are

evidence for trap mutation. On the microscopic level this mechanism was confirmed for the double vacancy site [21].

2.3 Temperature Programmed Desorption

Temperature Programmed Desorption (TPD) is also known as Thermal Desorption Spectroscopy (TDS). From TPD measurements concentrations and binding energies (E_b) of atoms and molecules adsorbed on the surface or retained in the bulk of a solid can be deduced. The method is commonly used in solid state surface physics. A detailed account of the underlying theory and devices needed is given elsewhere [25–27]. Here only an overview is given.

TPD is performed by heating a sample under vacuum and recording the effusion flux of the atoms or molecules of interest as a function of time. The effusion flux at any instance of a heating ramp depends on the amount of trace atoms, their implantation depth, sample temperature, trap concentration, detrapping and retrapping energies. From a TPD measurement information about these quantities can be deduced.

2.3.1 Theory of TPD

In order to analyze TPD data, a model describing the effusion flux from a sample is necessary. This requires an understanding of diffusion in solids and of vacuum physics.

Any kind of chemical processes are neglected in the following, as this work is about the noble gas He.

By setting up a rate equation of the molecules/atoms flowing in and out of the measurement chamber, it is possible to calculate the effusion flux (Φ) at any given point of the measurement if all other quantities are known. The rate equation is [4]:

$$\Phi + L = K\ S\ p + K\ V\ \frac{dp}{dt}. \tag{2.2}$$

Here Φ has the units of molecules/atoms per unit time. L is the leak rate under which all sources that emit molecules/atoms into the vacuum are collected, i.e., leakage through vacuum seals and desorption from the walls. It is given in molecules/atoms per unit time. S is the speed at which the system is pumped. It is usually given in liters per second. p is the partial pressure of those molecules/atoms for which the rate equation has been set up. V is the vacuum vessel volume. Lastly there is the coefficient $K = \frac{1}{k_B T}$ for the conversion of volumetric to particle flow.

Usually the quantity of interest is not Φ but $\frac{\Phi}{A}$, where A is the implanted sample area.

When inserting $L = K\ S\ p_{eq}$ (equilibrium pressure, p_{eq}, being the pressure which is reached after prolonged pumping, i.e., when the pumping capacity and the background stemming from desorption from the walls and minor leaks are in equilibrium) into equation 2.2, it can be solved as:

$$\frac{dp^*}{dt} + \frac{p^*}{\tau} = \frac{\Phi}{K\ V}. \tag{2.3}$$

Here τ is the system's characteristic pumping time which is defined as $\frac{V}{S}$, i.e., vacuum vessel volume divided by the pumping speed. Experimentally it is determined by measuring the time it takes for the pressure to drop to a fraction of e^{-1} of its initial value when no gas source is present. Furthermore $p^* = p - p_{eq}$ is the deviation from the equilibrium pressure.

As will be shown in section 3.3.5, for this work only the case where $\tau \ll dt$ is of interest, i.e., where the pumping time constant is much shorter than the measurement interval[1]. Based on equation 2.3 P.A. Redhead [4] derived a relation for the desorption from a unit surface. The relation accounts for a temperature dependence (exponential term) and considers concentration dependence where necessary:

$$\phi\,(t) = \frac{\Phi\,(t)}{A} = \nu_{a_m}\ \Theta^m\ \mathrm{e}^{-\frac{E}{k_B\ T}}. \tag{2.4}$$

Here Θ is the surface coverage, given as the fraction of trace atoms per surface atom. ν_{a_m} is the rate constant of the desorption process, a quantity equivalent to the attempt frequency, i.e., the frequency at which a trapped atom attempts to escape from the trap. The activation energy (E) is the energy of the barrier that needs to be overcome for the desorption process to take place. For an atom escaping from a trap the activation energy is called detrapping energy. m is the order of the desorption peak. Depending on whether it is a first ($m = 1$) or a second order ($m = 2$) desorption process, a different solution is valid. For a first order process the desorption rate is linearly surface concentration dependent, while for a second order process it is exponentially dependent. The drop off of Φ after its maximum is much steeper in a first order peak, therefore, it is possible to distinguish a first from a second order process by the peak shape. Another important distinction that can be derived from equation 2.4 is that the desorption temperature is independent of surface coverage for a first order peak.

For these analysis methods to be used, distinct non-overlapping peaks are necessary. The result is an equation system with activation energy and attempt frequency as unknowns. Therefore, at least two measurements with distinct[2] heating ramp rates are necessary in order to obtain a solvable equation system. In practice, however,

[1] for the system used in this work $\tau \approx 60\,\mathrm{ms}$.

[2] A minimum of two orders of magnitude difference is suggested [4]. In practice, the minimum

often the attempt frequency is assumed to have the value of the Debye frequency. The Debye frequency is the highest possible theoretical phonon frequency of a lattice. It can be easily calculated if the velocity of sound of a crystal is known [28]. While it is an "educated guess", experimental results for ν commonly deviate by more than one order of magnitude from this value [17, 29].

This model, however, holds only for adsorbates on or very close to the surface. For deeply implanted atoms the processes the desorbing species undergoes from the moment it becomes mobile to its desorption from the surface need to be considered. This process is usually diffusive in its nature. The average time it takes for an atom to reach the surface is readily calculated if the effective diffusion coefficient of the atom in the solid is known. The effective diffusion coefficient is a phenomenological parameter that changes with respect to the microscopic structure and temperature of the material. In a pristine lattice it is highest. D decreases with the number and depth of traps present because diffusing atoms re- and detrap on their way through the material. The more of these cycles occur the longer it takes for an atom to travel through a unit length of material. The trap depth has a similar effect, it extends the average time period that an atom is held in a trap. The effective diffusion coefficient will be a combination of all these influences.

In order to analyze a system with inhomogeneously distributed traps of distinct energy and occupation levels computational rate-equation codes are used. (The reader is referred to section 2.4).

2.3.2 Time- to Temperature-dependence Conversion

During a TPD measurement the effusion flux $\Phi(t)$ and sample temperature (T_s) are often recorded with respect to time. In order to interpret and compare measurements they need to be converted to effusion flux $\Phi(T_s)$ versus sample temperature T_s. During the conversion the total amount of desorbed atoms/molecules needs to be conserved, i.e., $\int_{t_1}^{t_2} \Phi(t)\, dt = \int_{T(t_1)}^{T(t_2)} \Phi(T)\, dT$. This is achieved by equation:

$$\Phi(T_s) = \frac{\Phi(t)}{\frac{dT}{dt}}. \tag{2.5}$$

For a linear temperature ramp this conversion results in a scaling, as $\frac{dT}{dt}$ is constant. However, for a nonlinear temperature ramp, $\frac{dT}{dt}$ will vary and therefore peak-amplitude ratios may change.

difference necessary depends on the accuracy of the particle effusion flux and the temperature measurement.

2.4 Rate-Equation Modelling

In order to correctly interpret a TPD spectrum of an atom species implanted below the subsurface layer, a computational analysis is required. Two types of codes can be used: Monte Carlo-based codes that follow specific atoms through a grid of traps in a probabilistic manner or rate-equation codes that solve sets of differential equations set up to include diffusion, de- and retrapping processes in the layers of a sample. In Monte-Carlo codes the computational power needed becomes large when the diffusion-step length is small compared with the sample thickness. Its precision depends on the accuracy of the potentials, that governing the jump probabilities, used as input and the number of particles (N) simulated. The relative numerical error scales with $\frac{1}{\sqrt{N}}$. For macroscopic samples consisting of N_A particles, rate-equation codes are at an advantage. The working principle of rate-equation codes and the specific code used in this work are briefly described bellow. For a detailed description see [30].

2.4.1 Working Principle

In a rate-equation code the sample is split into segments of finite size and a set of equations describing the change in trace element concentration over time in each segment is set up. The size of the equation system is given by $\prod_i(n_i)$ where n is the number of segments in the i-th dimension. Usually, a one dimensional system is used. The rate equation must contain a flux, a source and a loss term. The flux term is given by equation 2.1. The source term contains implantation rate and detrapping, while the loss term consists of (re-)trapping and losses at the surface. In these terms, a temperature-dependent detrapping model; the detrapping energies (E_{deT}); migration energy; attempt frequency; trap density; trap type; implantation conditions etc. need to be included.

The system is iteratively solved at each time step. This yields the evolution of trace atom concentration over time and sample depth.

2.4.2 TESSIM-X

TESSIM-X [31] is a one dimensional rate-equation code implemented in Mathematica [32] by K. Schmid to simulate TPD spectra of up to two different hydrogen isotopes effusing from W. Its algorithm includes traps occupied by multiple atoms and a change in trap energy with respect to occupation level. An example of TESSIM-X use is given in [33]. The rate equation solved (for one isotope) is the following:

$$\frac{\partial C^S(x,t)}{\partial t} = D(T(t))\frac{\partial^2 C^S(x,t)}{\partial x^2} + S(x,t) - \sum_{i=1}^{N_T}\frac{\partial C_i^T(x,t)}{\partial t}. \tag{2.6}$$

Here C^S and C^T are the solute (untrapped) and trapped hydrogen isotope concentrations. The diffusion coefficient D is given by:

$$D\left(T\left(t\right)\right) = D_0 \mathrm{e}^{-\frac{E_m}{k_B T(t)}}. \tag{2.7}$$

Via the source term $S\left(x,t\right)$ the hydrogen isotope concentration is introduced. The implantation parameters are: implantation range [m], straggling [m], duration of the implantation [s], the reflection coefficient [unitless] and the implantation flux $\left[\frac{atoms}{m^2 s}\right]$.

How the interaction of the two isotopes is implemented in the code is not discussed here, because in this work only the implantation and TPD of one isotope (^{4}He) was simulated.

2.5 Ion Beam Analysis

In the field of Ion Beam Analysis (IBA) MeV ions are used to probe matter. IBA methods can give information about the stoichiometry and areal density of thin layers and can be used to detect trace amounts of particles in a material. IBA gives reproducible and precise results [34] on an absolute scale [35]. It is considered as nondestructive, however, as will be shown later, it can cause substantial damage on the microscopic level. The types of IBA used in this work are Elastic Recoil Detection Analysis (ERDA) and Nuclear Reaction Analysis (NRA).

2.5.1 Theory

In an IBA measurement the sample is exposed to an ion beam and the particles (re-)emitted from the sample are detected. All information gained about the target is derived form the characteristics of the incoming and outgoing beam.

The following picture is used to describe the process that occurs in between: An ion with a given energy is incident on the sample, it neutralizes above the surface and travels through the sample, losing energy along the way by scattering processes with the material's atoms. This continues until the projectile stops within the lattice (it is implanted), leaves the sample or undergoes a nuclear reaction. The stopping power is the energy loss of an atom in a material. It is mainly dependent on projectile energy and the type of interacting atomic species. The probability for a scattering event is dependent on projectile and target mass and nuclear charge, their initial energies and the angle under which the event occurs. This information is combined to give the scattering cross section. It is usually given for a specific energy and scattering angle. There are both theoretical and experimentally determined scattering cross sections in use. Elastic and inelastic scattering processes are distinguished. Elastic processes can be described by Coulomb interaction (Rutherford model). This model is valid up to energies where the particles shortest distance during the scattering process

drops below the range of the nuclear force. For this case inelastic scattering occurs as the nuclei can be excited or nuclear reactions occur. The energy change (Q) and reaction probability are dependent on the specific reaction. Those nuclear reactions that produce light, highly energetic particles at distinct energies are of most interest as they enable the determination of depth profiles of trace elements in a material.

2.5.2 Elastic Recoil Detection Analysis

Elastic Recoil Detection Analysis (ERDA) is the method of choice when the concentration of light elements in a sample needs to be determined. ERDA is not dependent on using specific nuclear reactions as in nuclear reaction analysis. It can be used to detect any species of atom providing the projectile is heavier than the target atom. ERDA measures the atoms ejected by elastic collisions from a sample by incident ions in forward geometry. ERDA is particularly suited for detecting trace amounts of light elements in samples made of heavy atoms. By mounting a stopper foil in front of the detector, an ERDA setup can be designed to produce inherently background free data. This is achieved because the stopping power is proportional to Z of target and projectile, i.e., heavy ions are stopped preferentially. Therefore, a foil of sufficient thickness acts as a mass filter. It stops all reflected and ejected heavy atoms while the light atoms reach the detector. For heavy projectiles ERDA causes substantial displacement damage to a sample.

The ejection of light atoms as intended by ERDA occurs preferentially at small scattering angles. While in theory the scattering is elastic and, therefore, approximated by the Rutherford model, in practice the scattering cross sections deviate from this model [9] due to nuclear resonances. It is, therefore, necessary to use experimentally determined cross sections or reference samples with known content.

Experimental Setup

The setup used is located on the RKS beamline at IPP's tandem accelerator facility (see section 2.6 for more information on the accelerator). The layout of the setup is given schematically in figure 2.1a. Samples are transferred to the measurement chamber via a load lock. The sample surface-normal is placed at an angle of 75° to the incident beam. The semiconductor detector is placed at a 15° angle to the surface in a forward geometry. The total scattering angle is therefore $30 \pm 0.5°$. A slit-shaped aperture of 0.35 mm width is placed in the line of sight between target and detector at a distance of 24.8 mm to the former. The aperture has a step at one end. It is 1.65 mm on its short and 1.75 mm on its long side. The resulting solid angle was calibrated as 0.967 msr. Furthermore, there is a $4.66 \times 10^{19}\ \frac{atoms}{\mathrm{cm}^2}$ thick Ni stopper foil placed in front of the detector. The foil has roughness of $2.98 \times 10^{18}\ \frac{atoms}{\mathrm{cm}^2}$.

The fluence incident on the sample is determined by measuring the charge delivered

to the sample and the inner copper shield, which is biased to −240 V in order to suppress secondary electrons. A second shield, this one grounded, is placed around the first.

The ion beam is supplied by a tandem accelerator with maximum 3 MeV terminal voltage.

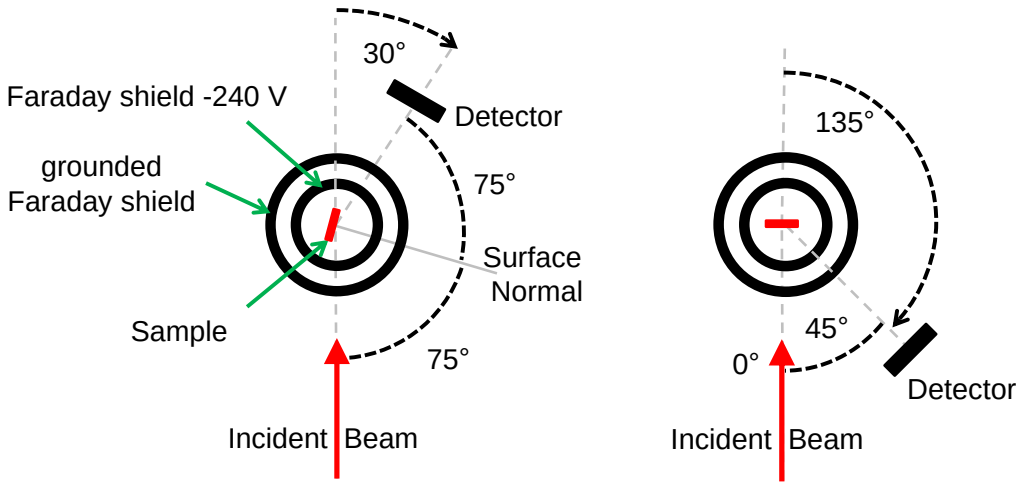

(a) **setup in ERDA configuration** $\theta = 30°$

(b) **setup in NRA configuration** $\theta = 135°$

Figure 2.1: IBA setup geometries used in this work and their scattering angles.

2.5.3 Nuclear Reaction Analysis

NRA is based on inelastic scattering processes between nuclei. For NRA nuclear fusion reactions are of interest. Target-projectile combinations are chosen that produce light particles at distinct high energies. This choice is made in order to produce probe particles deep inside the sample that carry information to the surface. Light, highly energetic particles are particularly suited for this as the stopping power (i.e. their energy loss per amount of material traveled trough) increases with Z and decreases with particle energy in the MeV range. As the stopping power and initial energy of the particle produced in the material are well known, the depth at which the nuclear reaction occurred can be deduced. Therefore, the energy distribution of the outgoing particle flux gives information about the total number and the depth distribution of the target atoms inside the material. In this work the D(^{3}He,p)^{4}He reaction is used to determine the D content of a sample. The energy produced in this reaction is 18.3 MeV. The reaction allows a W sample to be probed for D down to a depth of ≈ 8 µm for a primary ^{3}He beam energy of 4.5 MeV.

Experimental Setup

NRA is performed in the same measurement chamber as ERDA. However, the ion beam is incident along the sample surface normal and the detector is placed at a scattering angle of 135° (figure 2.1b). The detector is located 41 mm away from the sample and has a curved aperture of 35 mm width and 165.3 mm^2 area in front of it. Its calibrated solid angle is 77.5 ± 3.0 msr. All particles apart from the high-energy protons are prevented from reaching the detector by a foil, made of 50 µm Mylar coated with 50 nm Au, placed in front of the detector.

2.6 Sample Preparation

All samples used were cut from the same plate of tungsten (99.7 wt% purity) by spark erosion to a size of 15x12x0.8 mm. The plates were procured from Plansee SE. A detailed characterization and the description of the polishing and annealing process is given in [36] and [37].

In a first step all samples were mechanically polished with subsequently finer sandpaper down to an average SiC grain size of 5 µm until the remaining scratches were barely visible to the naked eye. Then, in order to obtain finer surfaces, the samples were electropolished in a 1.5 % NaOH solution. After this the samples had mirror quality. Subsequently, annealing was carried out for 2 min at 2000 K under vacuum, during which the pressure usually did not exceed 2×10^{-7} mbar. The annealing was performed in order to decrease the extrinsic defect density both by a reduction in the number of grain boundaries and by healing defects in the grains.

Helium Implantation Methods Used

The heat of solution of He in W is high compared to other light elements. It was calculated to be 5.47 eV [21]. This lies within the range of experimental results [1]. To overcome this energy barrier, implantations need to be carried out with a kinetic energy higher than this value. In order to span a large range of energies different implantation devices had to be used. All implantations were carried out at IPP. The implantation conditions of each sample prepared for this work are listed in table B.1 and B.2.

Low-Temperature Plasma

The device used for the 100 eV implantations is an electron cyclotron resonance (ECR) heated plasma device [38]. In this method a magnetic field (B_0) is applied to the to be ionized gas which is at the same time exposed to microwave radiation. The magnetic field is tuned to match the electron cyclotron frequency

$\omega_c = \frac{eB_0}{m_e}$. This creates a plasma in which the electron temperature is in the range of a few eV while neutrals and ions stay close to room temperature.

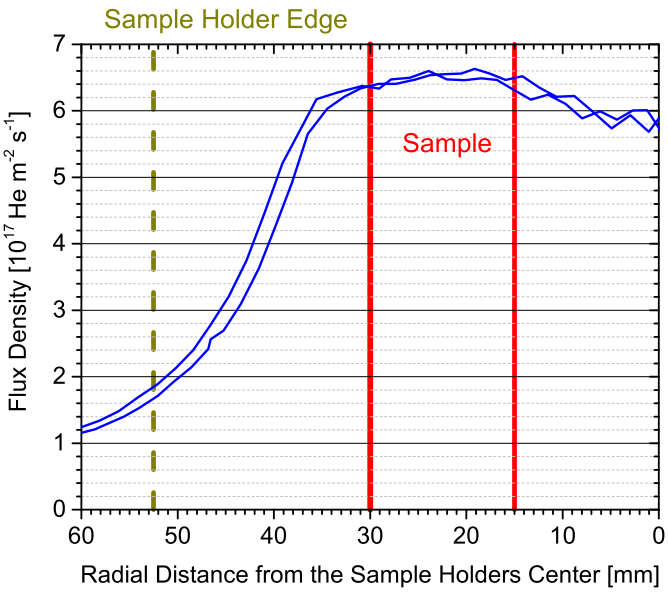

Figure 2.2: Radial distribution of the implantation flux of the low-temperature plasma source.

In the device the plasma is confined in a metal cage of 2.3 L volume. It has an opening of 5 cm on its bottom through which particles can escape and hit the samples 10 cm downstream. A manually operated shutter allows to control exposure time on the scale of 1 s. The ion energy is controlled by applying a bias voltage to the sample holder. The ion-flux distribution is determined by a double Langmuir probe mounted on a manipulator. It can be manually moved across the whole sample holder. A radial scan is displayed in figure 2.2. Here the Langmuir probe was moved in and out of the center of the plasma beam. In each implantation three samples were placed on the sample holder in a radially symmetric configuration. The ion flux only varies across the length of the sample, this variation is less than 10 %. At the same time the total ion current was determined by measuring the charge delivered to the sample holder. Following [38] a correction factor of 0.5 is applied to the measured current, in order to account for secondary electron emission. From the Langmuir-probe scan and charge measurement for a pure He discharge at 5.0 Pa and with a nominal microwave power of 90 W a flux of $6.5 \times 10^{17} \frac{\mathrm{He}}{\mathrm{m^2\,s}}$ was computed.

The sample holder temperature can be controlled by liquid thermostats in the range between 200 K and 800 K.

High-Current Ion Beam

Higher energy implantations were carried out in a high-current ion beam device. This device uses a duopigatron ion source [39]. The ions are extracted from the source by applying a potential of 6 keV. The ion beam is filtered using a bending magnet, i.e., only ions with a selected mass-to-charge ratio can pass. There are two biased cages placed around the sample holder in order to prevent secondary electron emission from influencing the current measurement. The current on the sample is measured by a charge counter connected to the sample holder and the inner cage. As of writing the level of accuracy of the current measurement is still under discussion, currently an under- or overestimation by a factor of 2 is possible. The beam spot area is $0.35\,\mathrm{cm}^2$. For 6 keV He, fluxes of the order of $2 \times 10^{18}\ \frac{\mathrm{He}}{\mathrm{m}^2\,\mathrm{s}}$ are achieved. Currently, only the description of the device's predecessor is available [40], a detailed description of the current device is due to be published soon [41].

High-Energy Ion Beam

High-energy implantations in the 0.3 to 0.8 MeV range were carried out using a tandem accelerator. The device uses an low-temperature RF-driven plasma as ion source. The positive ions are extracted into a lithium vapor cell where they are negatively charged. Before being fed into the accelerator they need to pass through a bending magnet. Here only ions of a specific mass-to-charge ratio band can pass. Next, the ions are attracted by the terminal voltage for the first time. Reaching the terminal, they are stripped off their electrons by collisions with nitrogen molecules. Now positively charged they are accelerated a second time. By this method the accelerator can use the same potential twice. The final ion energy is then given by $U_{accelerator} \times$(Ionization level after electron stripping + 1)e. There is a second bending magnet at the exit of the accelerator. This further reduces the mass-to-charge-ratio band $\left(\frac{mass}{q}\right)$ arriving at the target and allows the beam to be steered into the desired beamline. Fluxes are low compared with the other devices because of the higher number of loss channels.

The tandem accelerator used has a maximum terminal voltage of 3 MV. Therefore, He implantations at energies up to 9 MeV would be possible. The implantation flux is dependent, among other factors, on the energy chosen. For the implantations conducted for this work the time averaged flux ranged from $1.4 \times 10^{15}\ \frac{\mathrm{He}}{\mathrm{m}^2\,\mathrm{s}}$ for 0.3 MeV to $4.2 \times 10^{15}\ \frac{\mathrm{He}}{\mathrm{m}^2\,\mathrm{s}}$ for 0.8 MeV ions. The beam is scanned across the sample to achieve a homogeneous flux distribution. For a more detailed description of the implantation process the reader is referred to [42].

Chapter 3

Design and Commissioning of the High Temperature TPD Setup

The main goal of this thesis was to design, construct and commission a high temperature TPD setup, capable of fully desorbing He from W and thereby absolutely quantifying the He retention. This was achieved by upgrading the existing setup TESS (Thermal Effusion Spectrometry Setup). In this chapter first a description of the current setup is given. Then the design criteria for the new setup are derived in section 3.2, before the setup devised to fulfill them is described in section 3.3.

3.1 The TESS Setup

TESS is the main TPD setup of the plasma-material-interaction group at IPP and has been in use since 2002. Its center piece is a stainless steel ultra high vacuum (UHV) chamber with a quadrupole mass spectrometer (QMS). Both are described in detail in section 3.3. In addition to the newly installed high temperature heating unit and sample holder described below, TESS has an external oven that is slid over a glass tube containing a sample. Its T_{max} of 1300 K is sufficient for TPD of deuterium in W, however it is too low for helium TPD. Furthermore the fused silica glass of the tube is permeable to He at elevated temperatures. The He permeation rate increases in the temperature range from 273 K to 973 K by a factor of 200 [43]. The permeative flux though a barrier of 1 mm thickness is $\approx 2 \times 10^7 \ \frac{\mathtt{He}\ \mathrm{mm}}{\mathrm{cm}^2\,\mathrm{s}}$ at room temperature.

Additionally, there is a setup, which can also be connected to the TESS main chamber, whose centerpiece is an inductive furnace to heat samples for diffusion studies. The inductive heaters high power output allows large (many cm^3) samples to be heated to very high (> 3000 K) temperatures. Therefore it would also be suited for He desorption studies. The sample is situated in a water cooled quartz glass tube. This strongly reduces the amount of particles desorbed into the vacuum, as the chamber walls stay cold. However, it is not designed for a high sample processing rate. Instead the same sample is used for in situ loading and effusion studies.

3.2 Determining the Design Criteria

In order to perform meaningful high temperature TPD measurements on the He-in-W system, a setup needs to fulfill the criteria explained below.

3.2.1 Absolute Quantifiable Measurements

In order to enable the comparison with results obtained by other methods such as ERDA, the measurements need to be quantified on an absolute scale.

In order to obtain such results, the sensitivity, i.e., the partial pressure to signal ratio of the QMS, needs to be known for the relevant pressure range of 1×10^{-10} to 1×10^{-5} mbar. The same applies to the development of sensitivity with time. The former has been experimentally determined to be valid for TESS. The latter is done by repeating the calibration on a timescale that is short compared with the degradation rate of the detector (explained in section 3.3.6).

3.2.2 Accurate Temperature Measurement over the Full Ramp

An accurate temperature measurement over the full scale of the heating ramp is needed in order to determine the binding energies of He in W. A pyrometer would be the device of choice to measure a body at high temperatures because is does not require contact to the sample. However, pyrometers are effectively limited to high temperatures where the sample is much brighter than the surroundings. A thermocouple, on the other hand, is limited in temperature range by the alloy it consists of. Generally their measurement range ends well before their melting point. Furthermore, a thermocouple measurement is most accurate when the thermocouple is welded to the sample. This, however, complicates the sample loading procedure strongly, thereby conflicting with the requirement of a high sample processing rate. In practice, consequently, a compromise needs to be found, where the thermocouple is placed close to but not connected to the sample.

3.2.3 Minimal $4\ \frac{amu}{q}$ Channel Background

Since He is a noble gas that forms no molecules, it is predominantly detected as He^+ signal in the $4\ \frac{amu}{q}$ channel. The two main potential sources of background in the $4\ \frac{amu}{q}$ channel are singly ionized He^+ and deuterium (D_2^+). For He detection the He^{++} signal is negligible as the cracking ratio of He was experimentally found to be $\frac{He^{++}}{He^+} \approx 10^{-4}$.

He is present in the atmosphere at 5 ppmv [44]. The air leak rate in a vacuum system using copper seals is $< 1 \times 10^{-10}$ mbar. The glass viewports for vacuum systems have a similar maximum leak rate. Therefore, the partial He pressure in

a vacuum system due to air leakage would be orders of magnitude below this, thus neither detectable nor relevant. However, a second mechanism for He to enter a vacuum chamber exists, which is diffusion through solids. As mentioned in section 3.1 He permeation through glass is substantial at elevated temperatures. The permeation of He through steel is by orders of magnitude lower [45]. This is most probably not due to a low diffusion coefficient, but instead due to the energy of formation of He in steel being so large, that He from the atmosphere can not enter steel in relevant quantities in the first place. Therefore, steel is the material of choice for the vacuum vessel.

Two sources of D_2 background exists in the setup. Firstly, the natural isotopic abundance of $\frac{D}{H} = 1.6 \times 10^{-4}$ and secondly residual D_2 from previous measurements adsorbed at the inside surface of the vacuum vessel or retained in it. The retained D_2 is released when the vessel walls heat up.

Therefore, in order to keep the 4 $\frac{amu}{q}$ background low, precautions to keep the water background low and the heating as local as possible need to be taken.

3.2.4 High Sample Processing Rate

Naturally it is desired to have a high sample processing rate. However, inserting a sample requires the measurement chamber to be vented. This will degrade the vacuum due to gases, especially water vapor, adsorbing to the inside walls of the vacuum vessel, thereby possibly creating direct conflict with the minimal $4\frac{amu}{q}$-channel-background requirement. A compromise between sample processing rate and vacuum quality is required. Rebaking the vessel as part of the sample loading procedure is not an option, as this may alter the measurement results by premature degassing of the sample and lengthens a measurement cycle by days. A solution to this impasse is the use of a load lock, a prechamber to the measurement chamber. In this configuration, only the prechamber is vented, while the main chamber is constantly kept under UHV conditions. This eliminates the baking requirement, thereby greatly speeding up the sample processing rate. From the load lock a sample is transferred to the measurement chamber in a sample holder. The choice that has to be made is whether to measure the sample in this sample holder or to transfer it to another sample holder permanently installed in the measurement chamber and to retract the transfer arm. The latter solution leads to the least contamination while the former is easier to implement. A discussion of these issues and the description of such load lock setup is given in [46].

3.2.5 Maximum Temperature $> 2700\,\mathrm{K}$

A study by J. Pierre and D. Paulmier [47] using 3 keV He ions on W shows the highest desorption peak maximum of their measurement at 2650 K, with the peak's high-

temperature flank extending beyond the 2900 K temperature range of their setup. This high desorption temperature is in part due to their fast ramping rate (of the order of 30 K/s). If a ramping rate of approximately 1 K/s were to be used, it would be expected that this peak would shift to lower temperature. Such a lower heating rate would also be preferable from a measurement point of view, as it would decrease the overlap between desorption peaks. These findings are supported by studies of A.A. van Gorkum and E.V. Kornelsen who also measured incomplete peaks under similar implantation conditions and with a similar heating ramp rate [6, 7]. The main difference to the studies by J.Pierre and D.Paulmier is a lower maximum heating-ramp temperature (T_{max}) of 2400 K in A.A. van Gorkums study.

The highest detrapping energy of $E_{detr} > 5.2\,\mathrm{eV}$ [6, 47] derived from each of these measurements coincides with the highest detrapping energy found in modern density functional theory (DFT) studies [22]. From these findings, it was concluded that for He implanted at keV energies, a T_{max} of 2700 K is sufficient. That such a T_{max} is most probably also sufficient to desorb He implanted at MeV energies was shown in a recent study by Y. Gasparyan [48]. While in this study the amount of He desorbed from a sample with a 2 K/s TPD ramp up to 2473 K was negligible, an identical sample was fully degassed for the same ramp with an additional holding time at T_{max} for 30 min. In this study ^{3}He was used. This enabled the He content to be determined by deuterium NRA before and after the heating ramps. It was concluded that He is desorbed, albeit at a low rate, at 2473 K. Therefore, an increase in T_{max} to 2700 K is expected to raise the He's desorption rate sufficiently so that it desorbs during the ramp.

Lastly, the desorption peaks were simulated within this thesis by rate equation modeling. The results gained using ν_a close to the Debye frequency and $E_B = 5.1\,\mathrm{eV}$ (Figure 4.1) give a desorption peak few hundred kelvin of the value expected from previous experiments. It is not clear which experimental peak corresponds to it, therefore both an over- or an underestimation is possible. This large divergence is not surprising as the code does not contain part of the physics involved. A detailed description of the code and a discussion of its output is given in sections 2.4 and 4.1, respectively.

3.2.6 Sample Heating Rates in $5\,\mathrm{K/s} \geq R_{heating} \geq 0.05\,\mathrm{K/s}$ Range

The heating rate requirement is chosen to match the heating rates previously used in TESS for deuterium TPD ($10 - 0.05$ K/s) in order to be able to generate comparable data. Furthermore, experience with deuterium suggests that such heating rates produce desorption signals within the detection range of the QMS. Finally, the considerations made in the previous section make it clear that low ramp rates are desirable so that the He desorbs at low-enough temperatures.

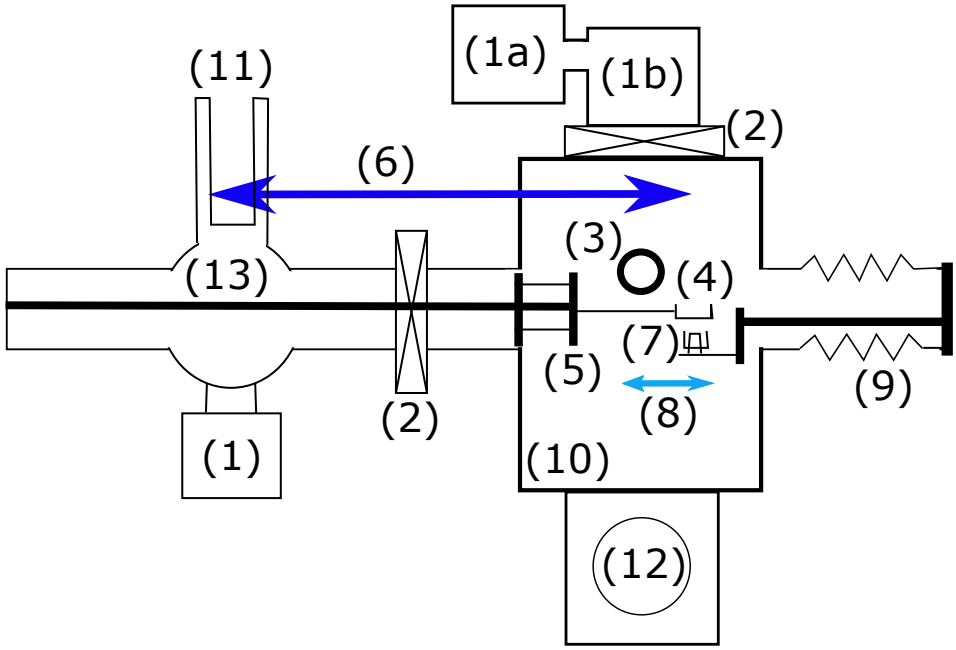

Figure 3.1: Vertical cut along the manipulator axis through the setup. (1) turbo molecular pumps, (2) gate valve, (3) quadrupole mass spectrometer, (4) sample holder, (5) heat shield on the manipulator head, (6) Δx of the sample holder, (7) electron source, (8) Δx of the electron source, (9) precision manipulator, (10) main chamber, (11) liquid nitrogen cold trap, (12) connection pipe to the inductive heater setup, (13) loading position.

3.3 Upgrading TESS

The main goal of this thesis was to make the existing TPD setup TESS capable of performing measurements of He implanted into W at up to MeV energies. In this section a detailed description of TESS after the upgrade is given.

In order to fulfill the design requirements explained in the previous section, most notably the $T_{max} \geq 2700\,\mathrm{K}$, it was decided to use an electron beam for heating the sample inside the main chamber of TESS. This type of heater was chosen over other methods such as inductive or radiative heating, due to its very high efficiency, focused energy delivery and fast response time.

3.3.1 Working Principle of an Electron Beam Heater

An electron beam heater accelerates electrons thermionically emitted from a heated filament onto a sample by applying a potential difference between the two compon-

ents. On impact the electrons' kinetic energy is converted to thermal energy in the sample. The sample temperature is then proportional to:

$$T_s \propto C_1 \ (I_{fil})^{\frac{1}{3}} \ \mathrm{e}^{-\frac{C_2}{(I_{fil})^{\frac{2}{3}}}} \tag{3.1}$$

T_s: sample temperature, I_{fil}: electron source filament current, C_1&C_2: constants; a derivation is given in appendix A.1.

This equation does not account for energy lost via bremsstrahlung or due to ionization of atoms in the path of the electron beam.

The ratio of bremsstrahlung power (P_γ) to total beam power (P_{e^-}) can be estimated by $\frac{\mathrm{P}_\gamma}{\mathrm{P}_{e^-}} = 10^{-9} Z U_{ac}$ where U_{ac} is the accelerating potential and Z the nuclear charge of the target atoms [49]. Given the specifications of the power supply to be used and a tungsten target, $\frac{\mathrm{P}_\gamma}{\mathrm{P}_{e^-}}$ is $\leq 4 \times 10^{-4}$ and therefore negligibly small.

The ionization cross section due to a collision with an electron has its maximum at 50-150 eV, depending on the molecule. A rough estimation, using the parameters of the setup from this work gives a pressure limit of $p < 1 \times 10^{-2}$ mbar for which ions make up less than 1% of the current. Since the pressure in TESS is in the range of 1×10^{-10} mbar to at very most 1×10^{-6} mbar, ionization losses can be neglected.

3.3.2 Mechanical Structure

Vacuum Vessel The setup is arranged around a cylindrical main chamber 435 mm in height. It has an inner diameter of 267 mm, resulting in a volume of 25 L. There are a total of 19 ports on the chamber. A load lock is connected by a CF63 flange. It is 340 mm in length and has a cold trap and a CF100 side flange in the setup plane, perpendicular to the loading path as shown schematically in figure 3.1. The sample holder is fixed to a magnetic manipulator ($\Delta x = 530$ mm). It is used to transfer the sample holder from the load lock to the main chamber. In the load lock samples are placed in the sample holder either via the CF100 side flange or from above via a 40 mm flange. The electron source is mounted on the flange opposite to that of the sample holder.

The other flanges of the main chamber are occupied by:

- connections to the inductive furnace and the glass tube heating systems
- the quadrupole mass spectrometer
- the electron source
- two turbo molecular pumps in series
- a pair of calibrated gas leak bottles

- viewing windows, including that of the pyrometer

Sample Holder In order fulfill the maximum temperature requirement the sample holder had to be made from tungsten. As tungsten is a hard and brittle material, neither the use of screws nor springs was possible. This severely limited the possible design choices. The new sample holder was therefore designed as a halfpipe made from a 0.05 mm thin tungsten sheet held in position by slits in a pair of tungsten rods as shown in figure 3.3. These rods are in turn mounted into a 62 mm diameter disc made of TZM[1]. The disc acts both as heat shield and structural component. As the disc is more than 120 mm away from the sample and there additionally is a W plate in the line of sight, it was possible to use a material with a lower melting point and more favorable machining properties.

The disc is connected by 60 mm long TZM rods to an identical disc which is in turn fixed to the tip of the manipulator. Apart from their function as structural components the discs also help fulfill the need to keep the pressure low. This is explained in detail in section 3.3.5.

The halfpipe z-axis is parallel to the manipulator axis. The W halfpipe has a circular hole at its center with a diameter of 13.0 mm. Samples are placed over the hole. This configuration allows the electron beam to directly reach the sample from underneath. The sample is placed in the sample holder with the He-implanted side facing away from the electron beam. This geometry is chosen to prevent a distortion of measurement results by electron-stimulated emission of He from the surface [50].

[1] TZM: Titanium(Ti) Zirconium(Zr) Molybdenum(Mo) Alloy - chosen for its favorable machining properties with respect to pure Mo or W.

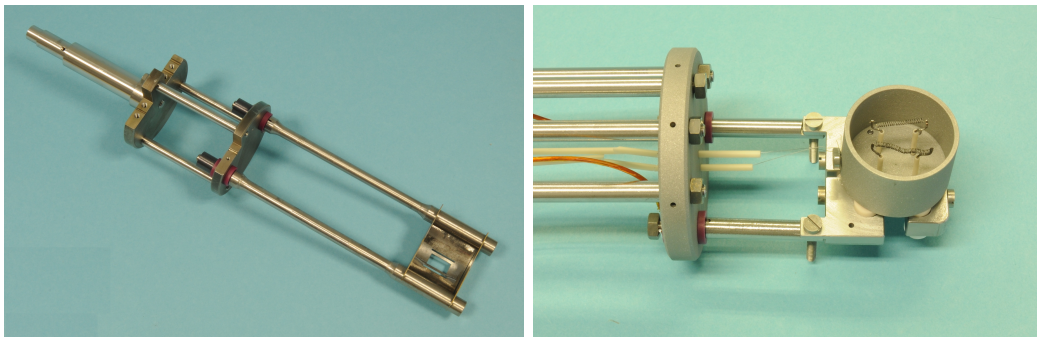

(a) Photograph of the manipulator head. (b) Photograph of the electron source.

Figure 3.2: Both photographs were taken before installation in the vacuum chamber. Note that the wiring is not yet fully installed.

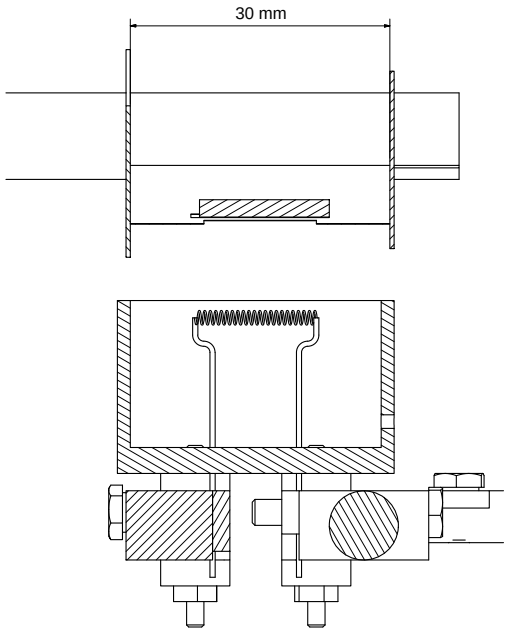

(a) Vertical cut along the manipulator axis through the sample holder and electron source. Wires are omitted for clarity.

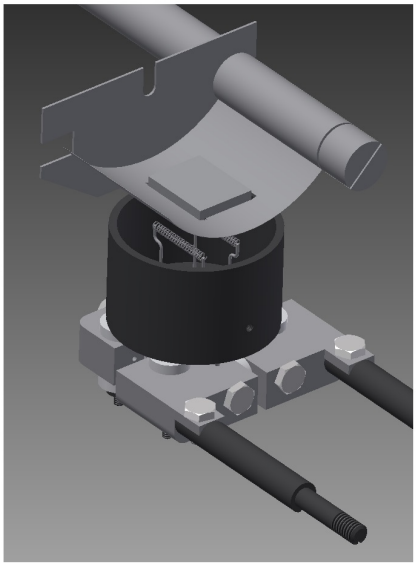

(b) CAD rendered view of the sample holder and electron source. The front parts are removed for better visibility.

Figure 3.3

The sample holder is electrically insulated from the heat shield and manipulator by ceramic spacers.

The spacing of the discs is chosen such that the sample can either be run in line-of-sight configuration with respect to the QMS aperture or 6 cm away from it to reduce the heat load on the QMS. Line-of-sight mode allows those atoms/molecules desorbing from the sample to be detected by the QMS, that are not re-emitted from the chamber walls.

A photograph of the sample holder before installation is displayed in figure 3.2a.

Electron source It is mounted on a Δx =100 mm precision manipulator on the flange opposite to the sample holder entrance flange. It is located in the plane below the sample holder. The manipulator is used to move the heater in and out of line of sight mode. Also it allows the electron beam position to be fine tuned. A photograph and the blue print of the electron source are displayed in figures 3.2b and 3.3.

3.3.3 Temperature Measurement

The sample temperature is measured using the combination of thermocouple and pyrometer.

Type C thermocouple: It consists of two wires made from two different rhenium (Re) tungsten alloys. The $\frac{Re}{W}$ ratios used for the wires are: 5% and 26%, respectively. The measurement range is specified from 273 up to 2573 K. The wires are hooked into a hole (diameter 1 mm) in the sample holder; therefore, although not being in direct thermal contact with the sample, the thermocouple provides a temperature reading that is proportional to that of the sample. The proportionality can be seen in figure 3.4. Together with the temperature measured by the pyrometer, it can be retroactively converted into the temperature values of the sample at $T < 1273$ K. Its error is given by the manufacturer as < 4.5 K up to 698 K and, above this, as 1% of the measured value.

The pyrometer[2] gives a reading starting from $T > 1273$ K up to 3573 K. It measures at a wavelength of 1.27 µm. At this wavelength the emissivity of tungsten ($\epsilon = 0.33$) is temperature independent in the range from 1600 to 2800 K [51]. As the measurement is performed on electropolished, therefore very smooth samples [36], which have in addition been recrystallized, the effect of surface roughness can be neglected. A reference measurement was carried out by G. Holzner [52] using the induction heater setup of TESS. The results showed excellent agreement of the pyrometer temperature reading with a type C thermocouple laser welded to the sample. A detailed description of these reference measurements is given in appendix A.2. The pyrometers viewing angle onto the sample surface is $< 50°$ from the surface normal. The intensity of thermal radiation increases with viewing angle. The magnitude of this change is dependent on the wavelength emitted. The longer the wavelength is, the stronger is the angle dependency. Using an empirical relation for angle dependence, it was calculated that the sample temperature is overestimated by no more than 2.4% due to the viewing angle deviating from the surface normal [53].

Sample Temperature As mentioned, the thermocouple does not measure the sample temperature, but the temperature in its proximity. In order to avoid a discontinuity in the temperature measurement, the thermocouple value is scaled to match the pyrometer temperature. This is done by finding the parameters of the function:

$$T_{fit}(t) = a \times T_{tc}(t) + b \tag{3.2}$$

[2] SensorTherm: Metis M3

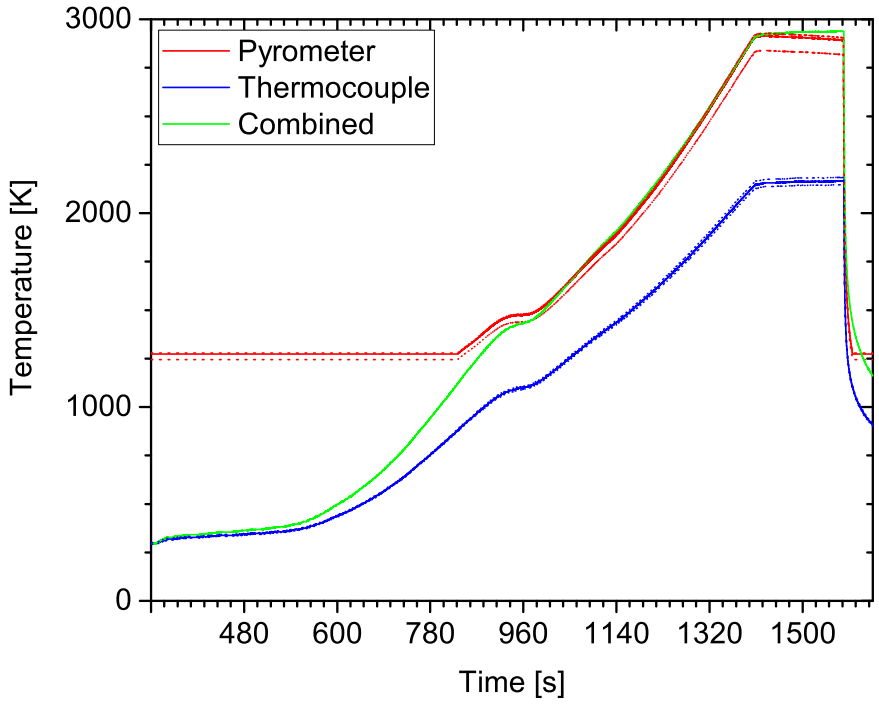

Figure 3.4: The graphs show temperatures measured by thermocouple (blue) and pyrometer (red) during a heating ramp. The green line represents the temperature ramp obtained by adjusting and combining both measurements. This is the temperature ramp used for analyzing the effusion-flux data. The dotted lines are the confidence intervals as given by the manufacturers. For the pyrometer additionally the maximum possible error due to angle effects is included.

with boundary conditions:

$$T_{fit}(0) = T_{tc}(0) \tag{3.3a}$$

$$T_{fit}(t_{transition}) = T_{pyro}(t_{transition}) \tag{3.3b}$$

The sample temperature is then taken as T_{fit} for $t < t_{transition}$ and T_{pyro} for $t > t_{transition}$. A sample heating curve displayed in figure 3.4 shows T_{tc}, T_{pyro} and T_{fit} with respect to time. The onset of the electron current is at approximately 500 s. At 950 s there is plateau visible both in the T_{pyro} and T_{tc} curve, it is attributed to an alteration in heat flow between sample and sample holder. From 1400 s to approx-

imately 1600 s the current through the electron source filament is held constant until it is finally switched off. In this time interval the temperature stays approximately constant. The steep dropoff in temperature after the filament current is switched off demonstrates that thermal inertias of the sample and holder are small.

3.3.4 Heating Unit

Heating of the sample is performed using an electron beam. Two filaments made from thoriated tungsten wire are used as they have a lower work function and thereby a higher electron yield at any given temperature (see equation A.8), in comparison with commercially available tungsten carbide filaments [54]. These custom made filaments also have the advantage that they are tailored in size to match the sample when mounted next to each other. The filaments are set in series, since the power supply used[3] has an I_{max} of 5 A. The two filaments combined consume $\approx 100\,\mathrm{W}(3.75\,\mathrm{A} \cdot 33\,\mathrm{V})$ when a T_{max} of 2700 K is reached. The highest measured temperature during testing was $> 3000\,\mathrm{K}$.

The sample is held at a positive bias, while the electron source is grounded; thereby the emitted electrons are accelerated towards the sample. The power supply[4] allows for a maximum accelerating potential of 5.0 kV and power output of 3 kW. Therefore, the electron beam is limited to a maximum current of 600 mA by the power supply. In practice an accelerating voltage of 4.0 kV and a power output of 2 kW has proven sufficient to fulfill the maximum-temperature and ramp-rate specifications. This is shown in figure 3.8.

During tests using a prototype of the electron beam heater with a thin (tens of µm) W foil it was observed that at the onset of the electron current the beam shape represents a projection of the filaments. However, with increasing electron current ($I_{e^-} > 2\ mA$), it becomes a homogeneous ellipse, which covers the whole sample. To focus the beam and to minimize electron loss onto the chamber walls, a Wehnelt cylinder at floating potential is placed behind, and around the filaments.

To better understand the influence of the Wehnelt cylinder's position and the accelerating potential on beam spot size and geometry, simulations were performed using the ion tracing software SIMION[5] [55]. A simplified setup geometry is implemented and values for the electric potential of each component are defined in SIMION. With this information as boundary conditions it then solves the Laplace equation, thereby calculating the shape of the potential field from which the electron trajectories are derived. SIMION was used to get a feeling for the expected trajectories and test multiple designs. As a final step, a simplified CAD model of the setup geometry was used as input geometry for a simulation in IBSIMU [56] by K. Schmid. IBSIMU

[3] FUG - NTN 350-65
[4] Technix - SR5KV-3KW
[5] version SIMION 8.1.1.32-2013-05-20

was chosen, because, as opposed to SIMION, it can take into account space charge effects properly. Also CAD files can be directly imported as the setup geometry in IBSIMU. The result shows that all electron trajectories coalesce in a small area at the center of the sample (figure 3.5). Therefore, the fraction of electrons expected to impinge on the sample holder is very small.

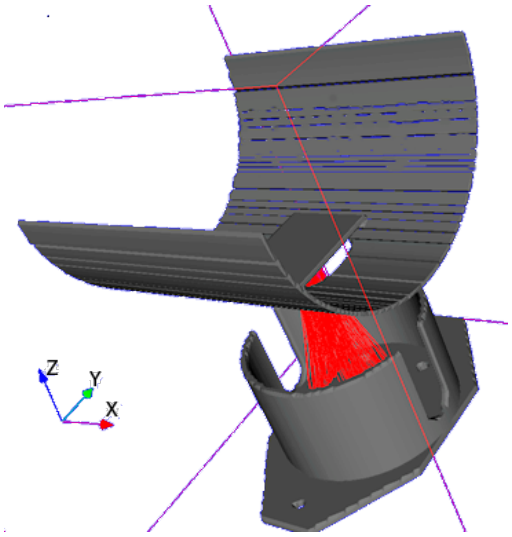

Figure 3.5: Visualization of a heater design study with electron trajectories (red lines) as calculated by IBSIMU for $U_{ac} = 100\,\mathrm{V}$.

Since there is a stable, quasilinear dependency (equation 3.1) of electron source filament current (I_{fil}) to sample temperature (T_S) for $T_S > 600\,\mathrm{K}$ an open loop control system is used, i.e., there is only a feed-forward control of the current through the filaments. I_{fil} is ramped up linearly. This avoids the use of a potentially unreliable temperature measurement as control parameter for the controler.

3.3.5 Vacuum System

The system is designed to minimize the background pressure in the main chamber. Vacuum is maintained by three turbo molecular pumps, two of which are mounted in series on top of the main chamber[6]. The third is mounted on the load lock[7]. Furthermore, the pump labeled (1a) in figure 3.1 has a Holweck stage, which gives it a largely improved hydrogen compression ratio with respect to a standard pump. Based on the vessel volume (V) and nominal pumping speed (S) of the main turbo molecular pump, the system's pumping time constant $\tau = \frac{V}{S}$ is calculated to be 30 ms. An experimental determination gave values of 50 ms for D_2 and 64 ms for He. As can be seen in figure 3.6, these values are close to the time resolution of the mass spectrometer. Furthermore, the accuracy of the determined pumping time constant values is limited by the manual operation of the gas-source valve.

Baking the main chamber and its adjunct parts from the outside at $\approx 190\,^\circ\mathrm{C}$ for ≈ 3 days reduces the base pressure down to $\approx 1 \times 10^{-10}$ mbar, as this speeds up the desorption of water from the vessel walls.

[6] This is a two stage setup consisting of a Leybold - Turbovac 1000 C, with a Leybold - Turbovac 90i as prepump.
[7] Pfeiffer - TMU 071

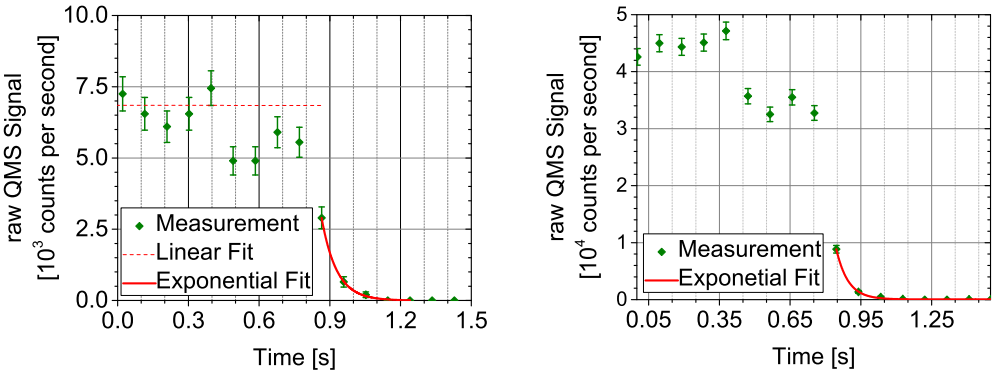

(a) QMS during the closing of the He leak bottle. $\tau = 64\,\mathrm{ms}$.

(b) QMS during the closing of the D_2 leak bottle. $\tau = 50\,\mathrm{ms}$

Figure 3.6: Experimental pumping constant determination by QMS scan during the closing of a leak bottle. The QMS is set to its highest possible time resolution. The emission current of the ionizer filament was set to 0.1 mA. The exponential fit from which τ is determined is shown in red.

Recontamination of the main chamber is minimized by keeping any newly inserted sample in the load lock for at least 12 h. Then the liquid nitrogen (LN) cold trap is activated which reduces the total pressure and the water related background by a factor > 2, as can be seen in figure 3.7. Only after the cold trap has been active for 0.5 h, the load lock and main chamber are connected and the sample is transferred.

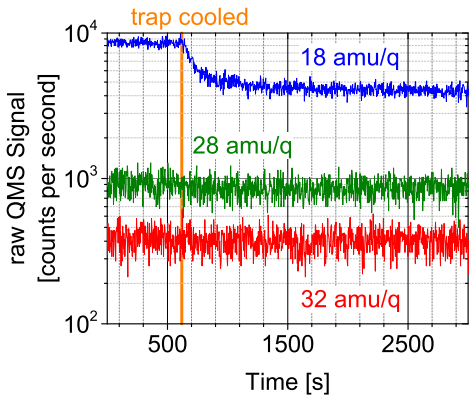

Figure 3.7: QMS scan during the filling of the cold trap in the load lock with LN.

In order to minimize the contamination due to particles entering the main chamber from the load lock, the sample holder is designed to minimize the molecular conductance between the two. This is achieved by the two metal discs (Ø62 mm), at least one of which is in the transfer pipe (Ø63 mm) when the sample holder is in position for a measurement to take place. They each narrow the pipe down to an approximately 1x200 mm slit. This reduces the pressure in the main chamber by $\approx 70\,\%$ and allows a ratio of $\frac{p_{Load}}{p_{main}} > 50$ to be maintained.

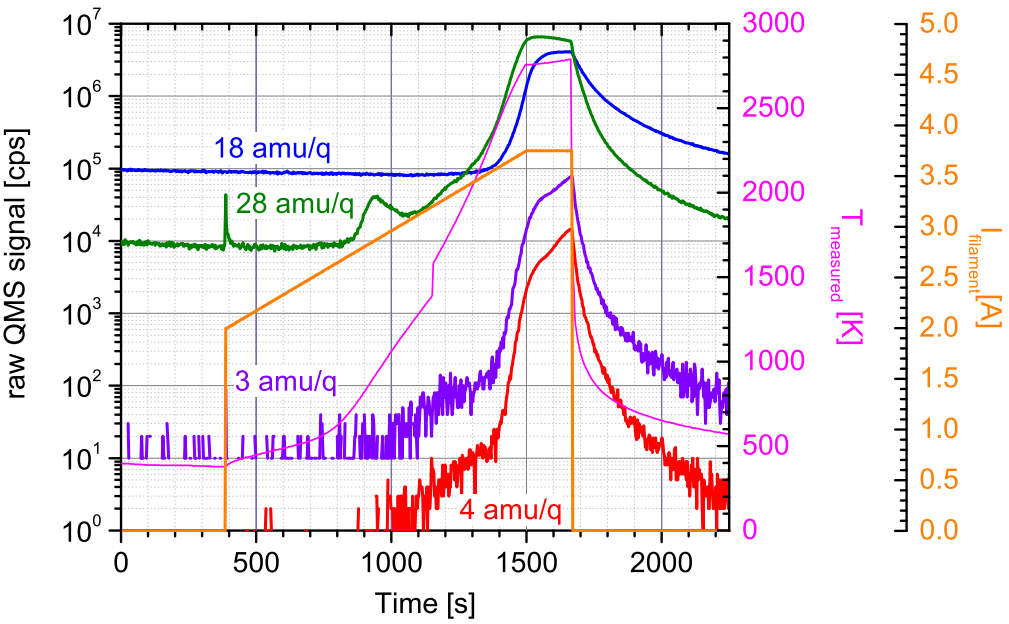

Figure 3.8: QMS raw data for four selected mass channels, $T_{measured}$ (pink) and I_{fil} (orange) during the heating ramp of an "empty", i.e., unimplanted W sample.

3.3.6 Mass Spectrometry Measurement

The particle effusion fluxes are measured by a quadrupole mass spectrometer (QMS)[8] with a cross-beam ion source. Its aperture is placed at the center of the measurement chamber. The QMS has a water cooled housing to mitigate the effect of a heat source in close proximity. Furthermore, the sample holder and heater can be placed such that there is no line of sight between QMS aperture and sample.

The QMS is calibrated by precision leak bottles using either helium (leak rate (L) = $4.93 \times 10^{-6} \frac{\text{atoms*cm}^3}{\text{s}}$) or deuterium (L = $1.32 \times 10^{-6} \frac{\text{molecules*cm}^3}{\text{s}}$ - their respective signal height can be seen in figure 3.6). The QMS sensitivity can be regulated by changing the emission current of the ionizer filament. This value has to be chosen such that: a) The 4 $\frac{amu}{q}$ signal is as high as possible. b) The detector does not saturate. This was achieved by a value of 0.1 mA in this work. When set to this value, the sensitivity is of the order of 1 count per second per 1×10^{10} $\frac{\text{He}}{\text{s}}$. However the secondary electron multiplier's (SEM) electron yield decays with the number

[8] Pfeiffer/Inficon DMM 422

of particles it has registered. A new calibration is, therefore, performed after each measurement. The development of the effusion for four selected mass channels during the heating ramp of an empty sample is shown in figure 3.8. The signal relevant for He, the $\left(4\ \frac{amu}{q}\right)$ channel has an acceptable ($<$ 10 cps) background up to 2400 K. From there on it rises exponentially.

Of the mass channels shown in the figure (3, 4, 18, 28 $\frac{amu}{q}$), channel 18 is predominantly H_20^+. Channel 3 and 4 stem from HD^+ and D_2^+. Note how these rise in unison as first the sample and then later the surrounding surfaces heat up. In the channel 28 signal, the switching on of the electron source filament is clearly visible as spike at $t = 400$ s. In the same channel an undetermined N_2 or CO desorption peak is present around $t = 950$ s. Finally, it is noteworthy that the detector saturates above 2×10^6 cps and hence the signal in channel 18 and 28 saturates when the peak temperature is reached. In a normal measurement cycle this must be avoided as a) data gained from such a measurement is incomplete, b) detector degradation is largely accelerated.

Chapter 4

Results and Discussion

In this section the results of both measurement and simulation are presented. Of the samples discussed, all but one were implanted to fluences $< 2 \times 10^{21}\,\mathrm{He/m^2}$ where no blistering was expected [57]. This threshold was confirmed in the experiment here as only the sample implanted to a fluence above the threshold showed blistering visible to the naked eye. It was attempted to perform all implantations at room temperature. Due to experimental constraints the 100 eV implantations were carried out at 300 K and the 6 keV implantations at 325 K. The sample preparation and the implantation devices used are described in section 2.6. A list of all samples measured in this work is found in appendix B.

4.1 Modelling

Before any experiments were conducted, He TPD spectra were simulated using the current knowledge base as input for the rate-equation code TESSIM-X (described in section 2.4). The effusion flux from He-implanted samples was modelled. The input parameters used are those given in table 4.1 if no other values are explicitly mentioned. Most of the values are taken from computational studies. A linear heating ramp starting at 300 K going up to 2600 K at a rate of 2 K/s is used in all simulations.

In figure 4.1 the effect of a variation in attempt frequency (see equation 2.4) on the effusion spectrum is displayed. The values are varied over four orders of magnitude, from the value suggested by van Veen (2×10^{15} s^{-1}) [18], over a value obtained from molecular dynamics (2×10^{13} s^{-1}) [22], to down below the Debye frequency ($\nu_{\mathrm{Debye}} = 8.1 \times 10^{12}\ s^{-1}$) of tungsten. From the figure the importance of using the correct attempt frequency becomes clear, as the 5.1 eV desorption peak is shifted by > 500 K from ≈ 1950 K to ≈ 2500 K, depending on which attempt frequency is used. Integration over the simulated desorption spectra from figure 4.1 yields a decrease in He retention by 12 % for a four order of magnitude increase in ν_a. In the following simulations ν_a is fixed at 1×10^{14} s^{-1} as it lies between the extremes.

In order to study the effect of a variation in incident He fluence, implantation with 0.8 MeV He followed by a heating ramp was simulated for four different fluences.

parameter	value	units	note
He implantation range	1.13	µm	^{a*}
straggling of He	2260	Å	^{a*}
reflection coefficient	0.0026	unitless	^{b*}
layer thickness	1, 0.3, 1, 100	µm	-
discretization of layers	10, 10, 10, 10000	nm	-
activation energy	5.0, 3.1, 3.0, 2.9, 3.0, 2.6, 2.3	eV	^{c}
attempt frequency	1×10^{14}	s^{-1}	^{d}
fraction of traps per W atom	30, 300, 1, 1	10^{-5}	$^{a\ e}$
migration energy	0.12	eV	^{f}
diffusion coefficient	2.5×10^{-8}	$m^2\ s^{-1}$	^{f}
flux	1×10^{18}	He m^{-2} s	^{g}
heating rate	2	K s^{-1}	-

Table 4.1: Parameters used for the TESSIM-X calculations. A more extensive table that includes the names of the variables as used in the code is given in appendix B.3.
[a]Range tables in SRIM-2008.04 [58].
[b]W. Eckstein's reflection tables [59].
[c]Density functional theory calculation from [22] figure 6.
[d]This value was chosen as it lies between 2×10^{15} s^{-1} given in [18] and 2×10^{13} s^{-1} calculated by molecular dynamics in [22]; both are higher than the Debye frequency, which is 8.1×10^{12} s^{-1} for tungsten.
[e]Damage profile calculated with SRIM and scaled to match the experimentally determined damage level.
[f]Ab initio calculation [60].
[g]Valid for the high-current ion source.
* Parameter valid for implantations with 800 keV He ions.

The result of this parameter scan from $7.7 \times 10^{18} \frac{\text{He}}{\text{m}^2}$ to $7.7 \times 10^{21} \frac{\text{He}}{\text{m}^2}$ is presented in figure 4.2. The fill-level-dependent detrapping energy manifests itself in the result of this simulation. At the lowest fluence traps are singly occupied and the He has the highest detrapping energy because the singly occupied trap requires the highest detrapping energy. For successively larger fluences the traps are filled with multiple He atoms and successively lower detrapping energies become available. Therefore, the high temperature peak grows first whilst the low-temperature peaks only follow with increased fluence. The retention is found to first increase from 34 % to 91 % (of the implanted He fluence) for the step from the first to the second lowest fluence. Then it decreases for each additional order of magnitude increase in fluence to first 73 % and then 9 %.

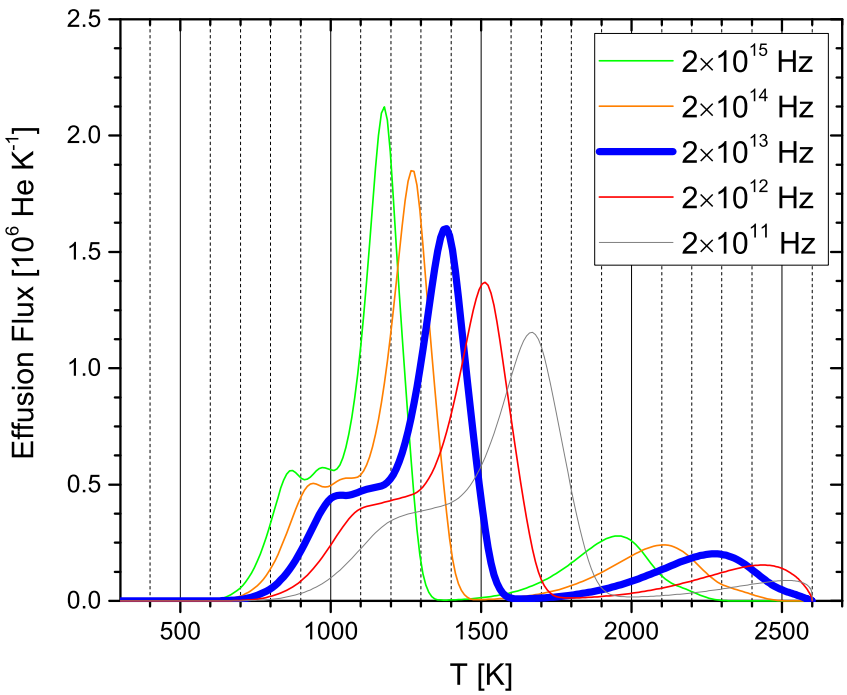

Figure 4.1: **Simulated desorption spectra** calculated with TESSIM-X for different attempt frequencies. All other parameters were held constant (See table 4.1) while the frequency at which an He atom attempts to escape from a trap(ν_a) is varied. The graph obtained when assuming a value close to the Debye frequency is displayed as a thick blue line.

The effect of a variation in ion energy was also simulated. The necessary change in implantation parameters for each of the three energies used is shown in table 4.2.

energy	reflection coefficient	range [Å]	longitudinal straggling [Å]
	[59]	SRIM-2008.04 [58]	SRIM-2008.04 [58]
50 eV	0.6920	5	15
1 keV	0.5073	32	70
800 keV	0.0026	11300	2260

Table 4.2: Implantation parameters used in the simulation displayed in figure 4.3.

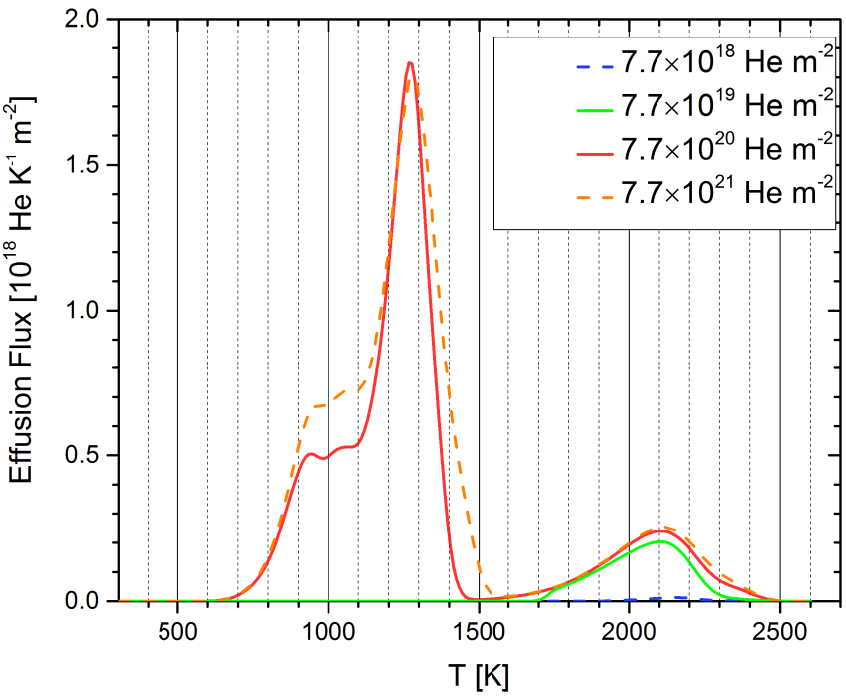

Figure 4.2: **Simulated He desorption spectra** calculated with TESSIM-X for various implanted fluences. The input parameters held constant are given in table 4.1.

The incident fluence was adjusted to balance the reflection coefficients' energy dependence, so that the amount of implanted He is the same for all energies. The results are plotted in figure 4.3. Although the implantation parameters were chosen to produce an equal amount of implanted He for each energy, the low energy implantations show orders of magnitude less He desorption and retention drops from 73 % to ≈ 3 % for the low energies. This is attributed to the difference in implantation range which increases the number of He atoms diffusing out of the sample for low energy implantation. Another interesting, albeit unexplained, result is that the high temperature peak is lower for the 1 keV than for the 50 eV implantation.

When comparing the retention in all simulations, the 800 keV implantation exhibit a retention more than two orders of magnitude higher than for the 50 eV and 1 keV implantations. Only for the highest fluence of the 800 keV implantations a smaller difference is observed.

When comparing the simulation results displayed in figure 4.1, 4.2 and 4.3 to

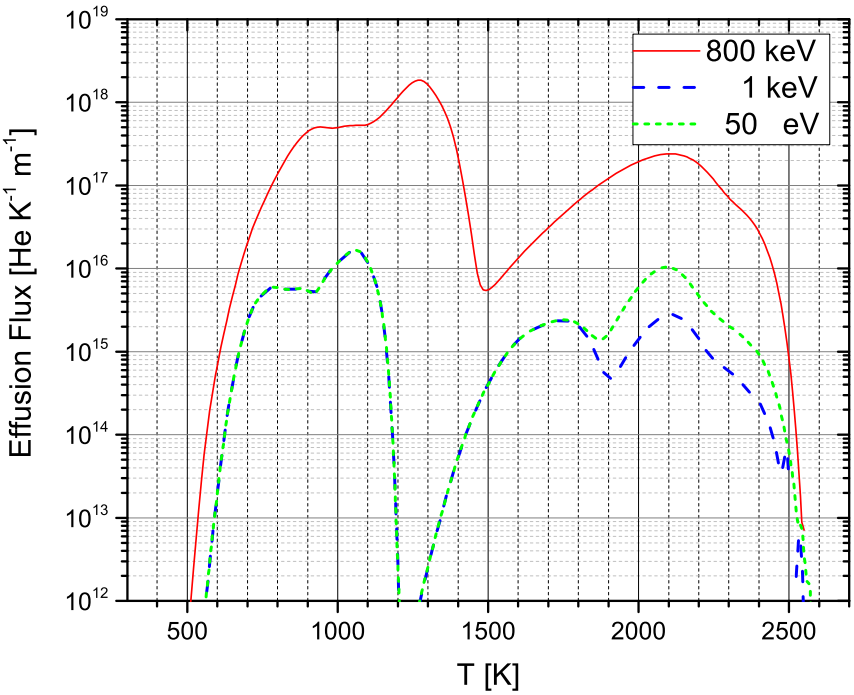

Figure 4.3: **Simulated desorption spectra** calculated with TESSIM-X for various implantation energies. The other parameters are held constant (See table 4.1) while energy and thereby the penetration depth of the incident atoms is varied. Only the incident fluence was adjusted in such a manner that the net implanted fluence was the same for all energies.

measurements from the literature, it becomes clear that they give no more than a qualitative estimate and the desorption peak positions are off by hundreds of degrees or are missing. He retention is at best qualitatively predicted, with results in the right order of magnitude. While this is unsatisfying, it was to be expected for a number of causes. These will be discussed in the following:

1. The parameters used to run TESSIM-X for He are mostly taken from computational studies, because they are not well or not at all known experimentally. For example, for the migration energy, values between 0.01 eV and 0.25 eV are given, depending on the study referred to. For the binding energies some values are known, however it is not clear to which exact detrapping process they

belong to. For the attempt frequency either assumptions (such as the Debye frequency) or computational values are used. These values can differ by more than two orders of magnitude.

2. TESSIM-X was designed to simulate hydrogen isotope implantation and diffusion. It does not contain some of the physics which is important for He implantation and diffusion in solids. Therefore, even if all input parameters were chosen correctly, the results would deviate from reality. For example:
   a) TESSIM-X uses fixed trap density distributions, it therefore
      i. cannot account for ion damage produced during the implantation
      ii. is oblivious to the concept of trap mutation which makes the capacity of traps increase with the amount of He trapped.
      iii. does not include mesoscopic phenomena acting as traps such as nanobubbles in its physics model.
   b) TESSIM-X calculates diffusion in the perfect lattice assuming jumps between tetrahedral sites, while for He it is unclear whether the path via tetra- or octahedral sites or a combination of both is taken [60, 61].
   c) only one trap type is implemented, however in reality several types of traps exist.

In conclusion, the results obtained with this incomplete physics model, the currently available set of input parameters and without any fitting to experimental results, at most provide a general idea about the relation of atomic-level parameters to the quantities measured.

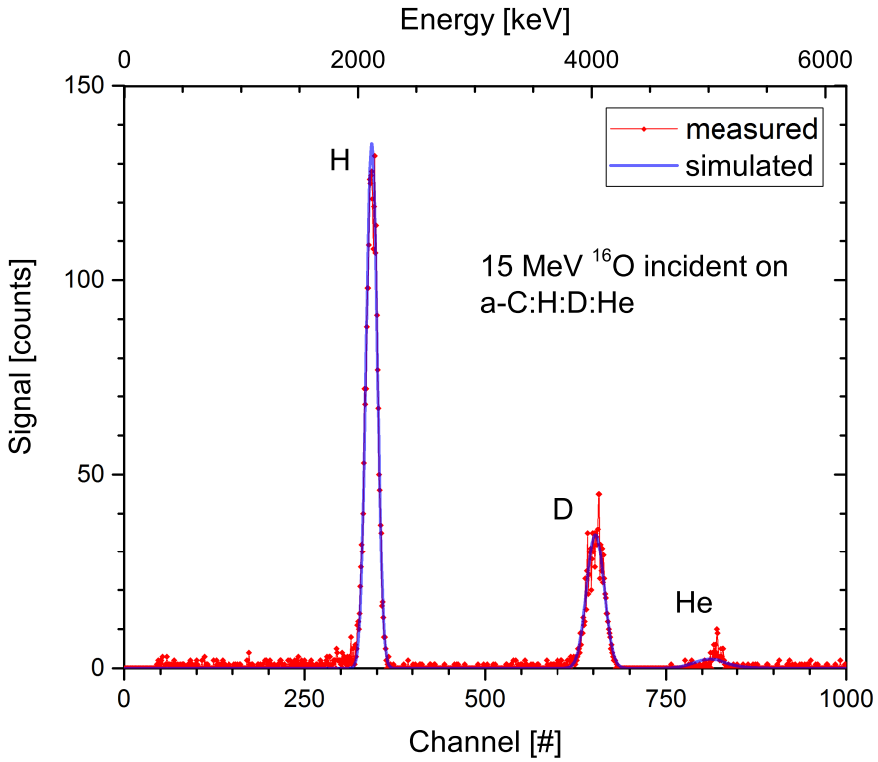

Figure 4.4: **ERDA Calibration Sample:** An amorphous deuterated hydrocarbon layer containing helium (a-C:H:D:He) is used to obtain the energy calibration.

4.2 ERDA Results

The absolute He content and its depth distribution in the sample were determined by ERDA. The measurements were conducted using the setup described in section 2.5.2. In order to absolutely quantify the measurement results a calibration sample was measured by ERDA and NRA first.

4.2.1 Energy Calibration

An amorphous, deuterated, He-containing hydrocarbon (a-C:H:D:He) layer plasma-deposited in an atmosphere of CH_4,CD_4 and He on a Si-wafer is used as calibration sample. In figure 4.4 the data obtained from this sample with a 15 MeV ^{16}O beam is displayed. The three peaks visible are H, D and He. Sputtered C and reflected ^{16}O are not detected because the are stopped in the detector foil of the ERDA setup.

Since the sample is only 53 nm thick, the thin layer approximation is valid, i.e., the layer thickness is below the depth resolution of the measurement and therefore the peaks can be treated as pure surface peaks. Therefore, when the channel number at the center of the peaks is plotted against the energy calculated for an atom knocked out of the surface, the channel number to energy conversion is obtained. Using this procedure with H- and D-peak position as input, an energy calibration was obtained. With this calibration it was discovered that the He is not in the hydrocarbon layer but at the interface to the Si. The result can be seen in the excellent agreement of simulation and measurement in figure 4.4. The fits displayed were calculated with SimNRA 7.00 [62] using the scattering cross sections presented in [9].

The measurement also displays the main advantage of ERDA, as here the different light elements present in the sample (H,D,He) are clearly distinguishable without background. The low level signal left of the H and D peaks is not noise, but trace concentrations of these elements in the Si substrate.

4.2.2 Absolute Quantification

The cross section data presented in [9] was used to analyze the ERDA data. These cross sections were originally obtained from SigmaCalc [63], i.e., obtained by using experimental data to determine the parameters of a scattering model that was then used to calculate the scattering cross section at the angle needed. It is known from comparison with experimental data (taken at $\theta = 170°$) that the calculated cross section reproduces all relevant nuclear resonances quantitatively [64]. However, the absolute quantitativeness still needs to be referenced independently.

Therefore, ^{3}He NRA was performed on the a-C:H:D:He layer. This method gives both an energy calibration and the absolute D content in one measurement. The result is displayed in figure 4.5. Three narrow peaks (labelled p_0, p_1 and p_2) from the ^{12}C(^{3}He,$p_{0,1,2}$)^{14}N nuclear reaction are visible, the one with the lowest energy is partially overlapped by the signal of ^{3}He backscattered from the surface. At high energies there is a broader peak from the D(^{3}He,p)^{4}He reaction. All four peaks were used to calculate the channel number to energy conversion using the same procedure as in the previous section. With the energy calibration known, the total D content of the sample was determined by fitting the D peak using the experimental cross section from [34] in SimNRA. The same was done for the D peak of the ERDA measurement. The cross section used for the latter was obtained from SigmaCalc [9, 63]. The NRA result is $1.77 \pm 0.10 \times 10^{21}$ D/m^2, while the ERDA result is $1.26 \pm 0.09 \times 10^{21}$ D/m^2. The error contains the statistical error (one standard deviation), a charge measurement error of 3 % and the error of the cross section which was assumed to be 5 %. The absolute quantitativeness of NRA with the D(^{3}He,p)^{4}He reaction has been confirmed by comparison to TPD measurements [35]. As NRA is known to be accurate within a few percent [34], all ERDA results given in the following are therefore the

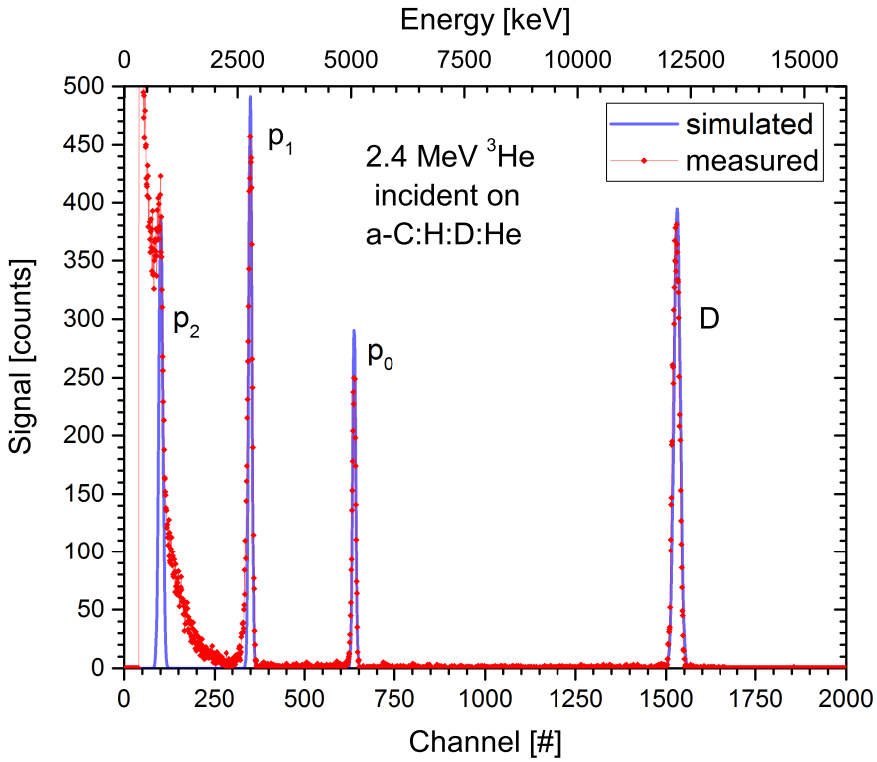

Figure 4.5: **The same a-C:H:D:He as in figure 4.4 measured by NRA**

measured values multiplied by a correction factor of 1.40 ± 0.13 derived from the NRA-ERDA comparison.

4.2.3 Measurement of He-implanted W

Four W samples, implanted with He at 100 eV or 6 keV, were selected for measurement with ERDA. No MeV range He-implanted samples were chosen as the implantation depth of He at these energies ($d_{He(300\,\mathrm{keV})} \equiv 500\,\mathrm{nm}$) [58] is larger than the ^{4}He detection range of ERDA ($d_{ERDA} < 500\,\mathrm{nm}$) [9].

The measured He peaks are displayed in figure 4.6. In this figure the signal counts are normalized to the amount of charge collected on the sample. The sample numbers (C0158 etc.) are given for later reference. Each peak was fitted with SimNRA. For the 6 keV implanted samples the peaks are non-Gaussian. The peak shape is evidence of the He not being limited to the surface region. It is further noteworthy that the sample implanted to $1.2 \times 10^{20}\,\frac{\mathrm{He}}{\mathrm{m}^2}$ with 100 eV He ions has its the 64 counts

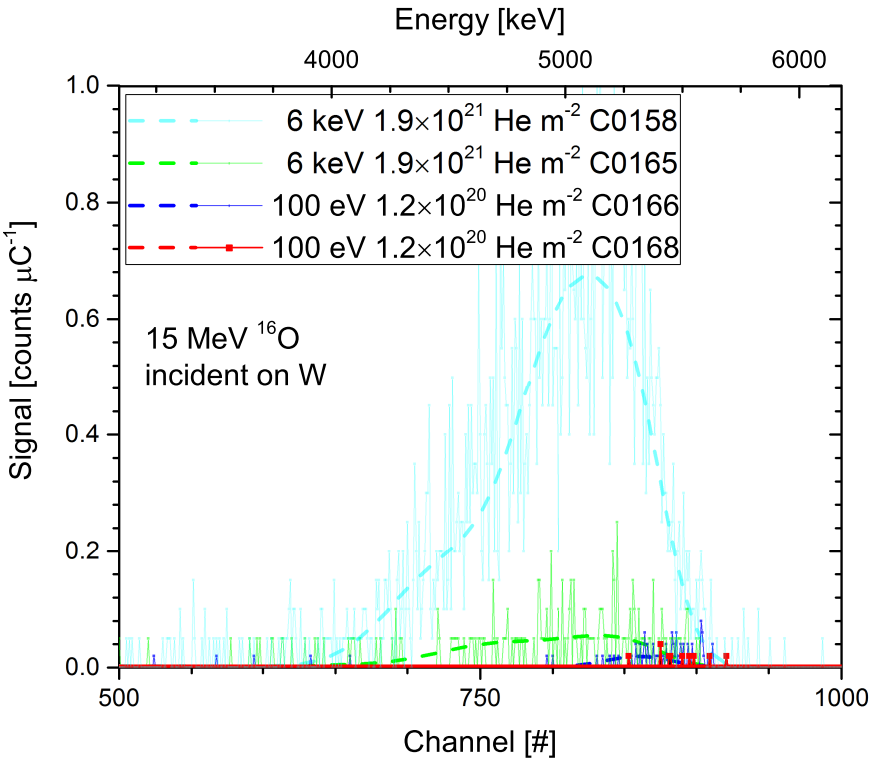

Figure 4.6: **ERDA** measurement (solid lines) and fits (dashed lines) performed with SimNRA[62] of four He-implanted W samples. The implantation energy and fluence are given for each sample. While there is a large variation in the signals strength even the weakest signal (sample C0168) is significant. More information about the implantation conditions is given in table B.1.

distributed over a range of 400 channels. This also is strong evidence for a low He concentration reaching deep into the sample. For the sample implanted with $1.2 \times 10^{19} \frac{\mathrm{He}}{\mathrm{m}^2}$ at 100 eV the detected signal comes exclusively form the near surface region. However, results for the latter sample are not conclusive, because even in the peak region the He concentration was close to the detection threshold.

The depth profiles corresponding to the SimNRA fits are displayed in figure 4.7. The error bars of the depth profiles given in figure 4.7 (and also of the absolute concentrations presented later in figure 4.16) contain an assumed charge measurement error of 3% for the ERDA measurement, its statistical error and the error introduced by the correction factor. Since all depth profiles go to zero before the maximum depth range of the ERDA measurement, it is assumed that all He retained in the

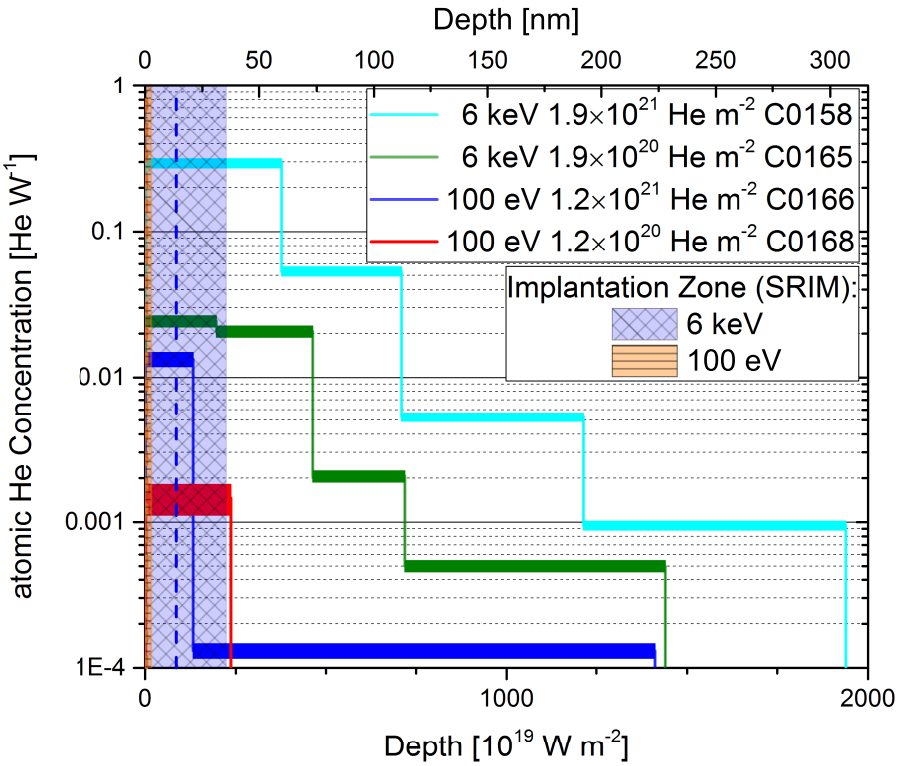

Figure 4.7: **ERDA He depth profiles** obtained from the fits in figure 4.6. Additionally the implantation range (dashed lines) and the implantation zones (patterned areas) as defined by the straggling both derived by SRIM are plotted.

samples was detected by ERDA. The width of the depth profile steps in figure 4.7 is within the depth resolution as calculated from ResolNRA [9][1], and therefore physically meaningful.

The presence of He up to a depth of nearly 300 nm is in stark contrast to the range and straggling, i.e., implantation distribution width, in W as calculated with SRIM. Figure 4.8 shows the predicted implantation profile for both cases. The range of the distributions is 0.7 nm and 13.6 nm, while their straggling is 2.0 nm and 21.7 nm, respectively.

[1] A repetition of the calculation from [9] with a more recent version of SimNRA that has a more accurate physics model can be found in appendix A.3.

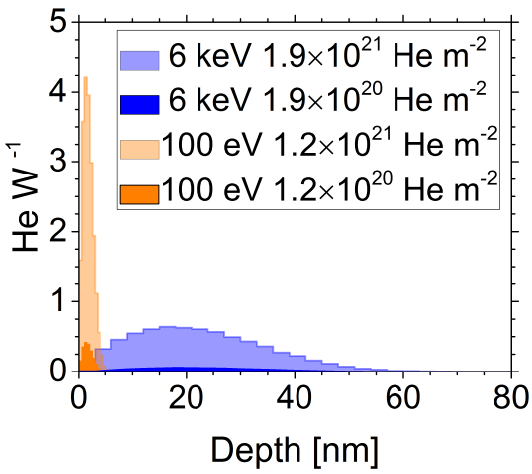

Figure 4.8: The He implantation depth profile calculated with SRIM in Kinchin-Pease mode is displayed.

4.3 TPD Results

Using the new setup described in chapter 3.3 four samples were outgased. These samples had been implanted in two implantation campaigns with 6 keV He ions at a flux of $2 \times 10^{18}\ \frac{\mathrm{He}}{\mathrm{m^2\,s}}$. Nominal incident fluence was $1.9 \times 10^{21}\,\frac{\mathrm{He}}{\mathrm{m^2}}$. One sample (C0169) was exposed to a higher fluence of $2.5 \times 10^{21}\,\frac{\mathrm{He}}{\mathrm{m^2}}$ to confirm the blistering threshold. Another (C0158) had been measured by ERDA before the TPD measurement.

The TPD measurements were conducted as follows: First the sample was placed in the load lock and pumped over night. Then the LN cold trap was activated. After waiting another $\approx$ 30 min the sample was finally transferred to the measurement chamber. Each sample was subjected to two heating ramps. The first to measure the effusion signal of He and the second to determine the background signal. The cool-down time in between was $\geq$ 3 h. The ramps were manually stopped just before the QMS would saturate. A calibration using a He leak bottle was performed after every ramp. The heating ramp used was approximately 1.0 K/s for all but one sample (C0156). Only for this sample it was faster; approximately 2.3 K/s. An overview of all TPD measurement results is given in figure 4.9. The error bars on the effusion-flux value represent one standard deviation. When absolute He content values are given, the uncertainty of the calibrated He leak bottle (8.0%)[2] is added. The temperatures displayed are calculated as described in section 3.3.3.

For further processing the temperature versus time curves shown in figure 4.9 were smoothed using a code provided by U. von Toussaint that implements a Bayesian spline fit [65]. The smoothed temperature curve was used to convert the effusion flux from time to temperature dependence using equation 2.5 presented in section 2.3.2. The resulting graphs are displayed in figure 4.10.

From the displayed measurements a number of observations are made:

1. The background is reproducible. Its onset temperature is proportional to the heating rate. In the measurement displayed in figure 4.9d the background measurement was aborted prematurely by a technical failure.

2. The temperature ramps of the initial measurements in figure 4.9a and 4.9c have plateaus. Their position is ramp-rate dependent. It is less pronounced for slower ramps. This is attributed to a change in heat conduction from the sample to the sample holder. Two possible mechanisms are that either the sample moves due to the thermal expansion of the sample holder foil or because welding occurs. Further evidence for the latter process is that the samples

[2] For Sample C0156 a deuterium (D_2) leak bottle was used. When a He leak bottle became available a conversion factor from D_2 to He calibration was experimentally determined. This measurement therefore also must take into account the D_2 leak bottle error. Their combined uncertainty is 9.4%.

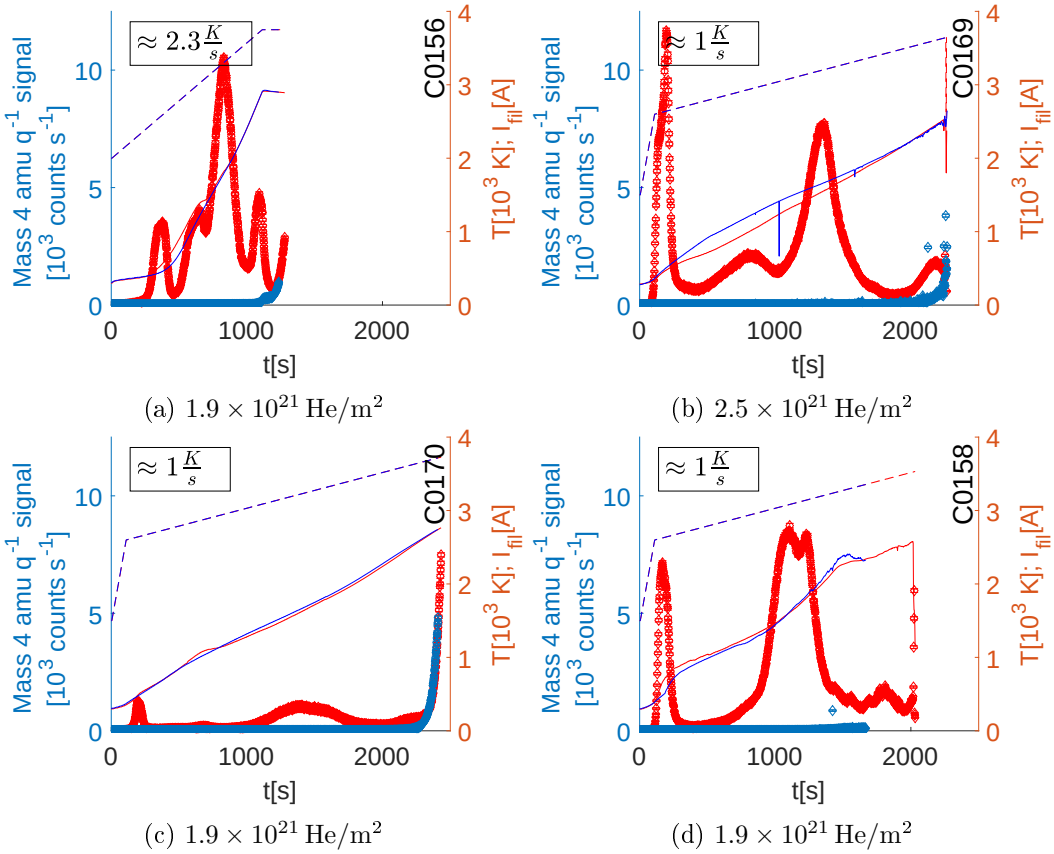

(a) 1.9×10^{21} He/m^2 (b) 2.5×10^{21} He/m^2

(c) 1.9×10^{21} He/m^2 (d) 1.9×10^{21} He/m^2

Figure 4.9: **TPD measurement data** as a function of time for 6 keV He-implanted W samples. Red is the first and blue is the second measurement of the same sample. The diamonds display the He effusion flux [He/s]. Its statistical error is smaller than the symbol size used. The dashed lines show the current passed through the electron source I_{fil} [A] and the continuous lines the sample temperature T [K].

"stick" to the sample holder after the measurements. Their bonding was sufficiently strong as to tear the foil when removing the sample. Spikes in the temperature measurements are hypothesized to be due to arcs that temporarily reduce the accelerating voltage. This reduces the power flux and makes the temperature drop instantly. In the measurement displayed in figure 4.9d, many small temperature spikes are visible. These are early indicators of the breakdown that lead to the abort of the second ramp in this measurement.

3. When a 1.0 K/s heating rate is used, all measured desorption peaks appear during the heating ramp. For the faster 2.3 K/s heating rate, however, additional holding time at the maximum temperature ($\approx$ 2900 K) is required before the last peak desorbs. Because the final peak for the 6 keV He-implanted samples appears only shortly before the exponential increase of the background, it was decided not to measure any of the samples implanted with He at energies two orders of magnitude higher. The He implanted in these samples has to diffuse a longer distance to the surface (1×10^3 nm compared with 2×10^1 nm for 6 keV implantations), therefore, the peak is expected to desorb after the exponential increase of the background. It is planned to measure these samples once the background has been pushed to higher temperatures by technical measures.

4.4 Notes on the Usage of the TPD Setup

Originally a total of 19 TPD measurements were planned. This number had to be reduced because the setup's high-voltage stability decayed quickly. This produced unsteady temperature ramps such as seen in the background measurements in figure 4.9b and 4.9d. When further tests using dummy samples were, made it was discovered that part of this problem was due to arcing. The arcs were found capable of evaporating part of the sample holder foil and disabling the thermocouple temperature measurement by overcharging it. When the sample holder and electron source were disassembled it was discovered that most of the insulating ceramics had been coated with metal by physical vapor deposition, i.e., the insulation had been short circuited. Subsequent chemical and thermal cleaning showed that the coatings mayor component was brass. However, other metallic deposits (Most probably W and Re) and carbon were discovered to. The brass was a residue from the spark erosion machining of the W components. After cleaning (by acid, sand blasting and heating) and replacement of some of the coated ceramics, the functionality of the system was restored for temperature ramps up to 2000 K. Above this temperature small drops in the temperature ramp continued to occur. During the renewed testing an increased signal in the 19 $\frac{amu}{q}$ channel was discovered. This was attributed to fluorine being released during the thermally induced decomposition of the polytetrafluoroethylene ("Telflon") coating of the high voltage supply cable. The 19 $\frac{amu}{q}$

channel can play an important for the quantification of deuterium desorption measurements, because in this channel HDO^+, a possible D-containing release product, is detected. As this was threatening to jeopardize the other TESS users measurements, any further repair attempts were put on hold.

While the brass coatings were a preventable one-time occurrence, evaporation of W and Re, and possibly also Mo and Al_2O_3 (although these components are further away from the heat source) will remain relevant issues. The insulator ceramics require periodic cleaning, because at the temperatures reached the materials used have vapor pressures that are significant. Even W has an evaporation rate of $1 \times 10^{19}\ \frac{atoms}{m^2\ s}$ at 2900 K. Furthermore, WO_2, which is present on any sample that has been exposed to air at a concentration of approximately $6 \times 10^{19} \frac{WO_2}{m^2}$ [66], will be fully evaporated during a heating ramp. The evaporation rates of the most relevant materials are given in appendix A.4.

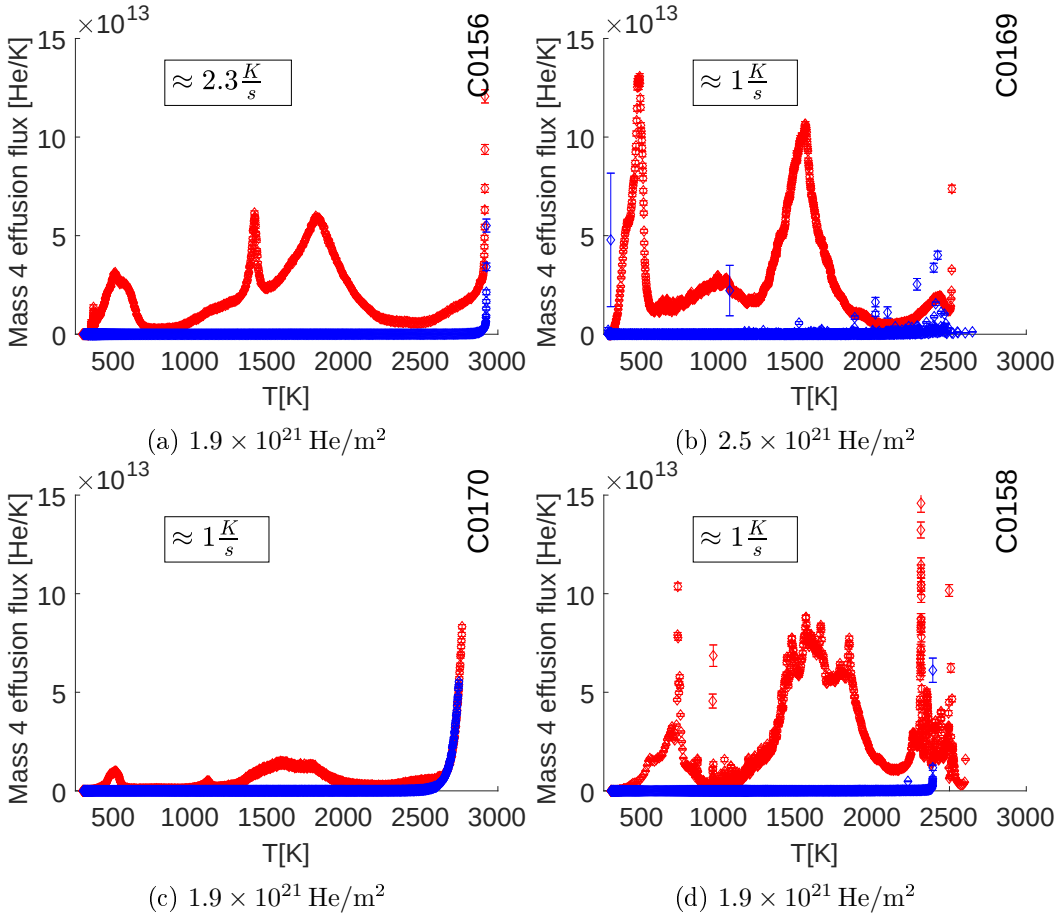

(a) 1.9×10^{21} He/m^2

(b) 2.5×10^{21} He/m^2

(c) 1.9×10^{21} He/m^2

(d) 1.9×10^{21} He/m^2

Figure 4.10: **TPD spectra from figure 4.9 as function of temperature.** The data were converted as explained in section 2.3.2. The red line is the first and the blue line is the second measurement of the same sample.

4.5 Discussion of Experimental Results

4.5.1 Desorption Peaks

Each TPD measurement presented yielded multiple He desorption peaks. In the following it will be discussed what information can be deduced from them. This will be achieved by comparing the He implantation conditions and TPD heating ramp settings to the peak configuration obtained.

All measurements yield a roughly similar peak pattern consisting of a well defined low-temperature peak with its maximum at around 500 K, a broad area spanning nearly 1500 K where most of the He effusion occurs and a peak just before the residual background saturates the QMS detector. First of all, in order to interpret figures 4.11, 4.12 and 4.13 correctly, the total amount of He retained in the samples needs to be discussed. The three samples compared were nominally, i.e., as measured by the charge counter of the implantation device, subjected to the same fluence of $1.9 \times 10^{21} \frac{\mathrm{He}}{\mathrm{m}^2}$. However, when integrating over the TPD spectra to determine each samples total He content, a discrepancy arises. Samples C0156 and C0158 have an identical He content within the margin of error. Sample C0170 however was found to have a He content amounting to 0.20 ± 0.04 of the other samples. This TPD measurement result is taken to be correct, because, as part of the standard measurement procedure, the measurement was calibrated to the absolute value of a He leak bottle after each ramp. The error is assumed to lie with the implantation source's charge measurement. This assumption is made for the following reasons:

1. The ERDA measurement confirms the TPD result for sample C0158.
2. Another sample exposed in the same separate implantation campaign as the outlier (C0170) to a higher fluence (C0169), also has a lower He content than expected. Albeit, its lack of retained He is not as pronounced as that of the outlier.
3. At the time of writing of this thesis the calibration of the implantation device was still under dispute.

This unfortunate deviation makes the following discussion of TPD spectra shapes more difficult, as the outlier was intended to be the reference sample. All comparisons are with samples from the first implantation series. Under these circumstances only peak positions, but not peak magnitudes, can be compared.

The low-temperature peak has been observed and discussed by E.V. Kornelsen. It is argued that this peak originates from a surface-related trapping site, because its amplitude is dependent firstly on the crystal face implanted and secondly on the amount of CO adsorbed at the surface [6]. In this work, a plateau-like structure (it

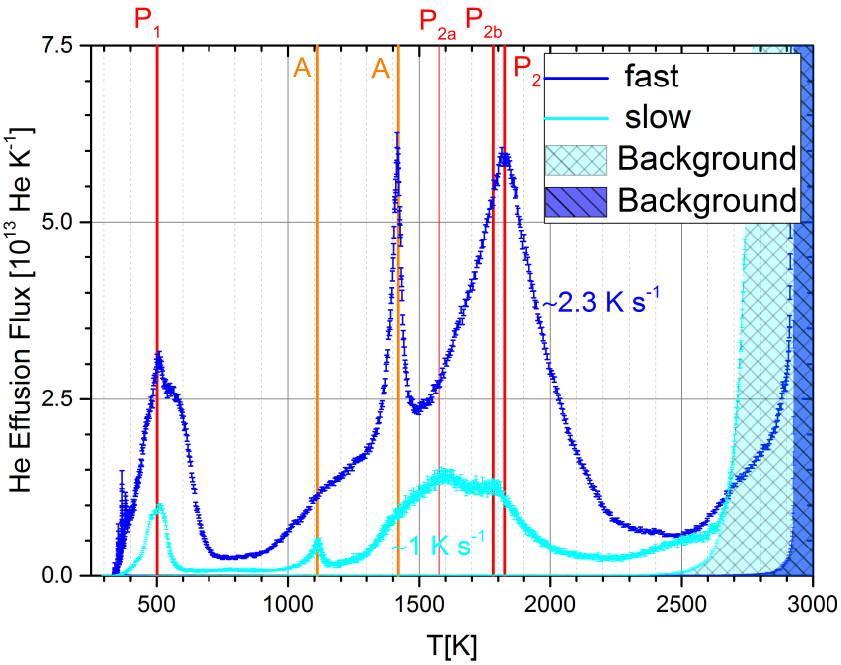

Figure 4.11: **Comparison of a fast and slow TPD ramp:**Both samples were implanted under nominally identical conditions. C0156 (dark blue) was TPDed with a ramp rate of $\approx 2.3\,\mathrm{K/s}$, while C0170 (light blue) was heated with approx. $1.0\,\mathrm{K/s}$

can be seen in the first peak of figure 4.11, a magnification of which is shown separately in figure 4.12) is observed that makes it likely that it consists of two or more overlapping peaks. In figure 4.12 these are seen to shift in desorption temperature in relation to ramp rate by $\approx 15\,\mathrm{K}$ for P1a and $\approx 65\,\mathrm{K}$ for P1b. The comparison in figure 4.13 of a TPD spectrum of a sample measured by ERDA, i.e., partially subjected to a $15\,\mathrm{MeV}$ $^{16}\mathrm{O}$ ion beam, to a sample not subjected to ion beam damaging, suggests that peak P1 is not due to a surface related site. In the spectrum of the ion-damaged sample the peak is delayed and broadened with respect to that obtained from the undamaged sample. This can be explained by retrapping of He, while diffusing to the surface, in traps generated by ion bombardment. The high-energy ion bombardment produced more traps ($1.2 \times 10^{22}\,\frac{vacancies}{m^2}$[3]) than the initial amount of He implanted ($1.9 \times 10^{21}\,\frac{\mathrm{He}}{m^2}$). As side effect of this delayed effusion the peak's double structure also becomes better visible. Since the ERDA measurements

[3]as calculated in SRIM using the Kinchin-Pease mode with 90 eV lattice binding energy.

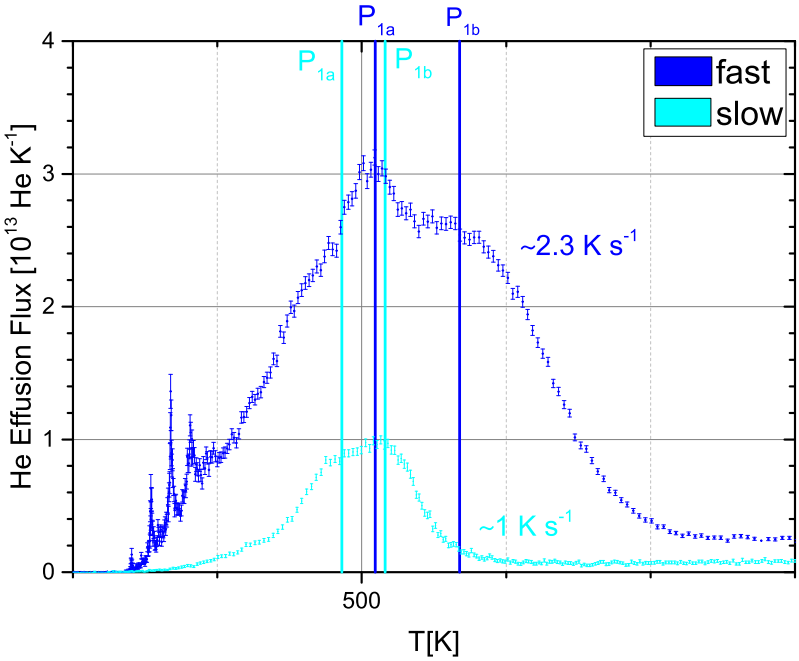

Figure 4.12: Detailed view of peak 1 from figure 4.11.

only affected about 33% of the implanted area, the TPD spectrum is in effect an overlay of the He effusion flux from a damaged and undamaged sample. Therefore, the onset of the first peak is still at the same temperature, while the first subpeak P1a is shifted by $> 50\,\mathrm{K}$ and subpeak P1b by $> 200\,\mathrm{K}$ to higher temperature. These details are clearly visible in figure 4.14.

In the central region reaching from $\approx 750\,\mathrm{K}$ to $\approx 2250\,\mathrm{K}$ in figure 4.11, a broad peak and, within it, a very sharp symmetrical peak are visible. The sharp peak does not represent any desorption energy level, but is created by a plateau in the temperature ramp. The plateau only occurs when a sample is heated for the first time after having been inserted into the measurement chamber. It is suggested that this occurs when the sample either moves or connects with the sample holder and by either of these processes the conductive heat flow from the sample to the holder increases. It occurs at $1100\,\mathrm{K}$ for the low $1.0\,\mathrm{K/s}$ ramp rate, but is delayed to $> 1400\,\mathrm{K}$ for the $2.3\,\mathrm{K/s}$ ramp rate. This is the case because under these conditions the total energy delivered to the sample - and therefore indirectly to the sample holder - is lower for any point in the measurement for the fast heating rate. Therefore the sample holder reaches a

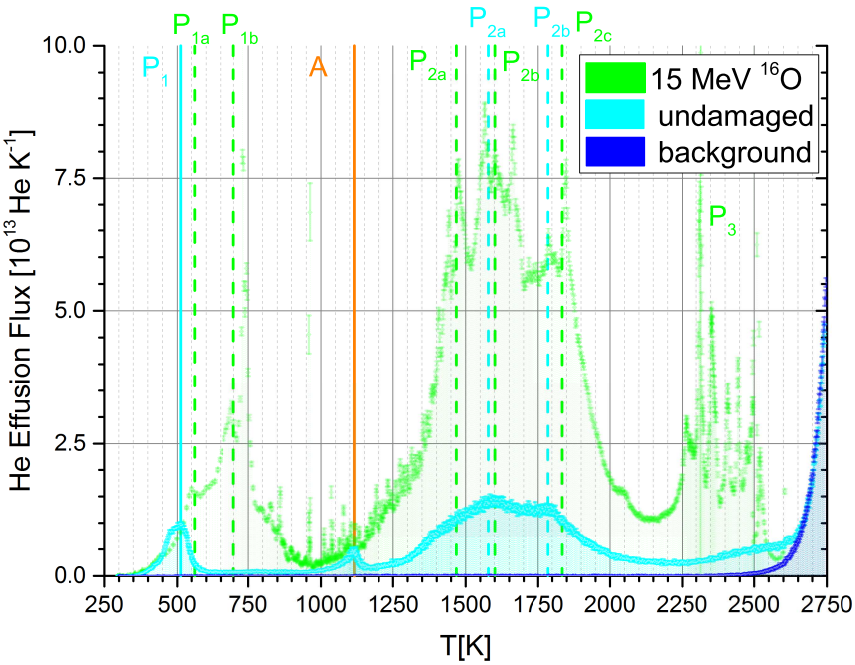

Figure 4.13: **Effect of ion damage on He effusion:** Both samples (C0158 and C0170) were implanted under nominally identical conditions and subject to heating ramps of the order of 1.0 K/s. Sample C0158 was in addition measured by ERDA before TPD, hence 33% of the implanted area was bombarded with 15 MeV ^{16}O ions, simulations with SRIM predict $1.2 \times 10^{22} \frac{vac}{\mathrm{m}^2}$ to be generated, the peak dpa is 0.2.

sufficient temperature for this binding process to occur, when the sample already is at a higher temperature.

When compared with TPD spectra from the literature achieving a similar temperature range, it is most noteworthy that, in contrast to most other high temperature measurements, in the spectra measured in this work there is no distinct peak structure. The only notable exception is a series of above displacement-damage-threshold implantations, where a structure similar to the low and mid temperature range in this work is seen [47, 67]. This is unexpected because in the literature a ramp rate of the order of 40 K/s was used, whereas in this work the ramp rate is < 2.5 K/s, so the peaks in this work should have been more distinctly visible. The shape of the peak does neither represent a first nor second order peak. It is suggested that this is the superposition of many peaks representing distinct binding energies. That the peak spans 1600 K implies a large number of possible detrapping energies. This observation

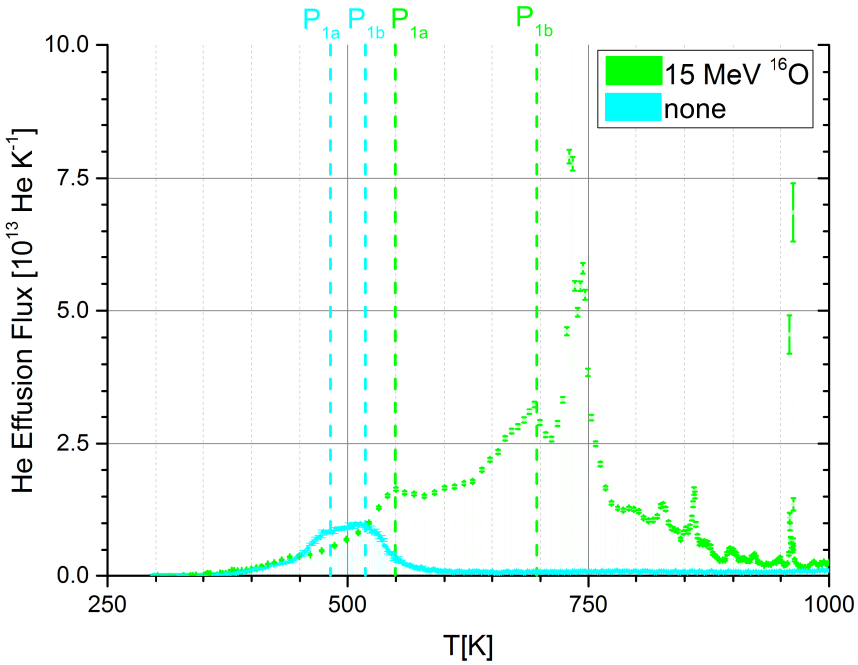

Figure 4.14: **Effect of ion damage on He effusion of the low-temperature peak:** Detailed view of the low-temperature peak displayed in figure 4.13.

is in accordance with the computational prediction suggesting a near continuous band of binding energies for He self-trapping in W in the $2.0\,\mathrm{eV} < E_{detrapping} < 4.0\,\mathrm{eV}$ range [22]. This implies that the He is in many multiply occupied trap sites, some of which might possibly be nano bubbles.

In the high temperature region, approximately 200 K before the 4 $\frac{amu}{q}$ channel background saturates the detector, another peak is visible. For the 2.3 K/s ramp its onset is at 2500 K and for the 1.0 K/s ramp at 2250 K. Of the measurements described in the literature, only one has potentially detected this peak [47, 67]. Even in that work it is questionable that this peak was detected as the heating rate used was 40 K/s, i.e., all peaks will have been strongly shifted to higher temperatures. More recently only Y. Gasparyan has shown a setup that is potentially capable of detecting this peak [48]. However, to date it has not been used on samples implanted with He at keV energies. The high temperature peak is probably due to helium detrapping from vacancies, when the $\frac{\mathrm{He}}{vac}$ ratio is < 2 [22].

This large spectrum of available binding energies prevented any peak from being distinctly resolved. Therefore, the detrapping energy and attempt frequency could

not be calculated for any trap. This also made it impossible to apply peak shape analysis.

The amount of He desorbed in each peak is compared with the total amount of He desorbed from a sample in figure 4.15. The fraction of He desorbed in the mid temperature range is within 0.72 ± 0.03 for all samples. The remaining He desorption is evenly split between the low- and high-temperature peaks. Only the sample implanted to a higher fluence (C0169) than the others shows a significant deviation from this pattern. Here the low-temperature He desorption is > 4 times larger than the high temperature desorption. This is attributed to a larger fraction of the retained Helium being trapped in blisters.

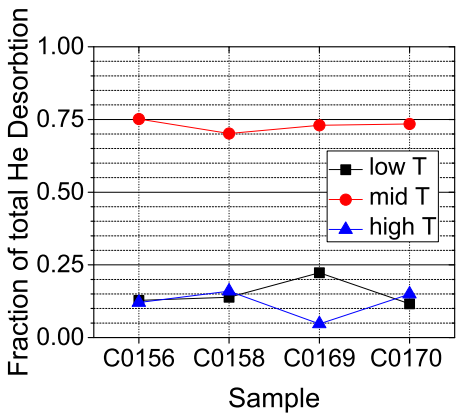

Figure 4.15: The fraction of He desorbed in a specific peak region with respect to the total amount of He desorbed is displayed.

Therefore, taking into account that, as explained previously, the usual TPD setup will not detect the high temperature peak, it is concluded that most literature values for absolute He content derived by TPD should be treated with care and considered as lower limits. This underestimation is expected to be higher for deeper implantations, as here there additionally is a shift to high temperatures due to the larger distance the He has to diffuse to the surface.

For the 6 keV implantations in this work the He content would have been underestimated by 5 % to 15 %. The results displayed in this work, however, have been shown to have complete He desorption, as the He content of the samples was determined prior to TPD by an independent method. The absolute He content value determined by ERDA matches - within the error bars - the value determined by the TPD measurement. As argued earlier, the retained He is all within the detection range of ERDA. From this the conclusion is drawn that all He is being desorbed during the TPD ramps.

4.5.2 He Migration Dynamics

When discussing the ERDA results, it is assumed that all He detected is retained in extrinsic trapping sites. This assumption is made because He in lattice sites - both octa or tetrahedral - has a migration energy that makes it mobile at room temperature. Therefore, all He in lattice sites will have effused from the sample by the time it was measured with ERDA days after it was implanted. The depth profiles

reach more than 250 nm beyond the implantation zones (compare figure 4.7 and 4.8), demonstrating the high mobility of an He atom in a W lattice before it encounters an extrinsic trapping site. The He depth profiles most notable feature is the lack of a diffusion front as a limited amount of traps would have generated. Instead the height and width of the distribution both increase with fluence, both for implantations below (100 eV) and above (6 keV) the damage threshold. Self trapping and trap mutation are good explanations for this behavior. They allow for an unsaturable reservoir of available trapping sites. The evidence for trap mutation seen in the 6 keV implanted samples is that here the He concentration found beyond the implantation range is well above the trap density of an annealed sample, which would be $< 10^{-5}$ W^{-1} [17]. The 100 eV implanted samples support this observation, as the concentrations in the surface layer are also higher than that of an annealed sample. However, in neither of the implantation series the exact magnitude of trap mutation can be determined because the layer with high He concentration is thinner than the depth resolution of the ERDA in this case. For the He detected deeper in the 100 eV high fluence sample, the concentration is too low to determine whether it is retained in traps belonging to the residual trap level of the sample or whether it is already in traps produced by trap mutation.

In order to facilitate the discussion of the behavior of the total retention, with respect to energy and incident fluence, the He content as measured by TPD, ERDA or NRA has been plotted versus the incident fluence in figure 4.16.

Both the total He retention as well as the maximum He concentration are higher for the 6 keV than for the 100 eV implantation. Even after taking into account the difference in incident fluence and the reflection coefficient, a factor of 12 for the low and 25 for the high fluence in the ratio between the retention of the 6 keV to the 100 eV implantation remains. There are two arguments to explain the lower retention for the 100 eV case. First, the implantation region is much narrower. Therefore, because the implantation fluxes for both energies are approximately the same, the initial He solute concentration is higher than for the 6 keV implantation. This leads to a higher He concentration gradient (∇N_{He}), which in turn means that the transport rate of He to the surface is higher. Second, the 6 keV ions generate vacancies, i.e., potential trapping sites during implantation. He is, therefore, more likely to get trapped and, thereby, prevented from diffusing back to the surface. The increase of the difference between above and below damage threshold implantations in retention with fluence is in part attributed to the ion damage. It is known to create a nonlinear increase in retention [6].

The maximum concentration of the 6 keV energy and $1.9 \times 10^{21} \frac{\mathrm{He}}{\mathrm{m}^2}$ implantation is 29 at.% vs. 2 at.% for the fluence that is by a factor of 10 lower. Firstly, this also supports the case made for retention increasing nonlinearly. Secondly, such a high concentration in a zone reaching from the surface 60 nm into the sample has been found to be an indication for the presence of nanobubbles [68]. The sample is close to

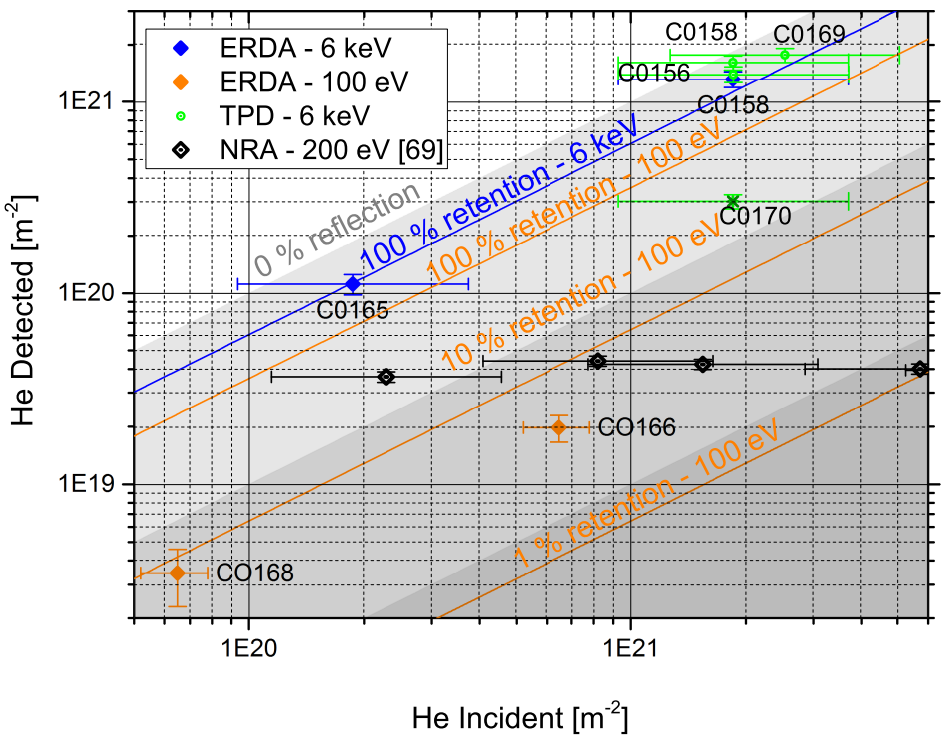

Figure 4.16: **Helium Retention Plot.** The absolute number of He measured during TPD is converted to $\frac{\mathrm{He}}{m^2}$ by dividing it by the implanted sample area. The upper limit values are obtained by using tabulated reflection coefficient values [59].

blistering. This observation fits with the discovery of blisters visible to the naked eye on the sample implanted up to a fluence of $2.5 \times 10^{21} \frac{\mathrm{He}}{\mathrm{m}^2}$ under otherwise nominally identical conditions and the blistering threshold known from the literature [57]. If the blistering regime has been reached, it would follow that the trace diffusion picture is not valid anymore in the blister containing layers. For the samples implanted with 100 eV ions no such distinction can be made, as the surface layer concentration determined is only a lower limit because of the limited depth resolution of ERDA. However, there exists a study using the same low-temperature plasma device as in this work to implant ^{3}He at 200 eV into polycrystalline tungsten samples. The retained amount of He was determined by deuterium NRA. It was found that for sub damage threshold implantations there is a fluence above which the He content saturates [69]. The lower limit for this to occur is $< 2.4^{+2.3}_{-1.1} \times 10^{20} \frac{\mathrm{He}}{\mathrm{m}^2}$. Therefore it is

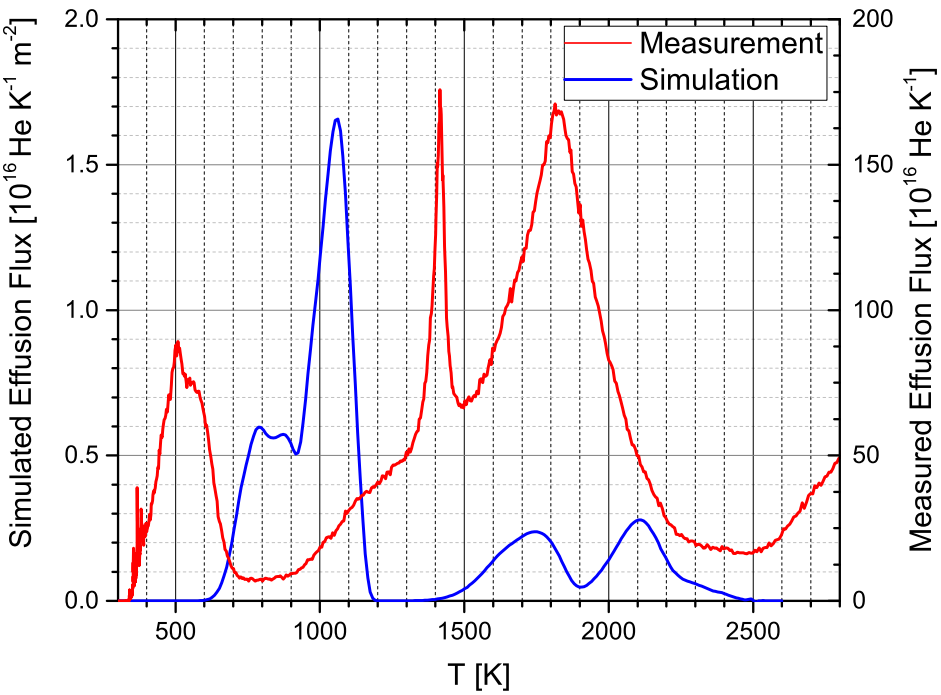

Figure 4.17: The comparison between a simulated (blue) and measured desorption spectra (red) is shown. The simulated spectrum is the 1 keV implantation taken from figure 4.3 while the measured one is the spectrum labeled 2.3 $\frac{\mathrm{K}}{\mathrm{s}}$ in figure 4.10a. The simulated spectrum is scaled up by a factor of 10^2.

most likely that the sample implanted with a fluence of $6.5 \pm 1.3 \times 10^{20} \frac{\mathrm{He}}{\mathrm{m}^2}$ of 100 eV He is also in this saturated regime.

4.6 Comparison of Measurement and Simulation

Returning to simulations discussed in section 4.1, which were performed before any measurement had been made, confirms that they were, as predicted, only qualitative. In figure 4.17 a simulated spectrum is compared with a measured one. The amount of He retained differs by about a factor of two. This is mostly accounted for by the difference in incident fluence. The relative retention is very similar although the implantation energy was by a factor of 130 larger for the simulated sample. However, TESSIM-X does not take into account displacement damage generation

during implantation. Therefore, a simulation of a 6 keV implantation has resulted in a retention one order of magnitude below the measured value. This confirms that the TESSIM-X results, with the here used parameters, can for the time being only be considered as a qualitative assessment. For the peak positions the situation is similar. TESSIM-X gives only qualitatively correct results. The low-temperature peak is not reproduced at all.

Chapter 5

Conclusion and Outlook

This work has shown that the dynamics of He in W present a topic that is both of purely scientific interest, as the dynamics of self-trapping and trap mutation are not fully understood yet, and at the same time of interest to the engineers designing a future nuclear fusion reactor.

A new setup for He TPD has been commissioned. It uses an electron beam heater to reach a maximum temperature of 3000 K. It has been shown that an open loop control system produces approximately linear temperature ramps in the $1\frac{\mathrm{K}}{\mathrm{s}}$ to $2.3\frac{\mathrm{K}}{\mathrm{s}}$ range. Mass spectrometry measurements have shown that the setup has an acceptable background in the 4 $\frac{amu}{q}$ channel for temperatures up to 2400 K. It was demonstrated by reference measurements with ERDA that the setup is capable of desorbing all He for implantation energies up to 6 keV. It was discovered that due to the high temperature achieved, the setup in its current form has to undergo maintenance on a regular basis. Otherwise a metallic coating builds up on the insulator ceramics that leads to a breakdown of the accelerating potential.

ERDA measurements performed complementary to TPD clearly showed the high mobility of He in W. Furthermore it became clear that He diffusion in W is not described by a diffusion front with a maximum concentration limited by the trap concentration. Instead, He distributions that increased in height and width with incident fluence and centered in their respective implantation zones were found. Also it was found that ERDA measurements had to be multiplied by a correction factor obtained by NRA. Only then did they match the TPD results. The deviation was attributed to the scattering cross section used. This cross section is based on the fitting of a scattering model to empirical data gathered at different angles. For more accurate data analysis it would be therefore advisable to obtain an experimentally determined cross section for the specific angle needed. Another path for more accurate ion beam characterization would be to use NRA instead. Here the $^{4}\mathrm{He}(^{14}\mathrm{N},\mathrm{p}_0)^{17}\mathrm{O}$ reaction, which has a set of resonances, could be used [70]. Furthermore ^{3}He can be implanted instead of ^{4}He, as its concentration can be very accurately measured by deuterium NRA. This, however, can only be an option to answer very specific questions which cannot be answered by TPD, ERDA or nitrogen NRA, as ^{3}He is scarce and expensive.

The TPD measurements of 6 keV implanted samples yield a very broad desorption band. This confirmed computational studies suggesting a combination of self-trapping and trap mutation to be occurring. Further, the low-temperature peak that was believed to belong to a surface related site was shown to contain at least one subpeak that is diffusion-limited, i.e., originates from the bulk. More than 85% of the measured He was seen to desorb from the low and mid temperature peak regions. The remainder was seen to come from a high temperature region above 2000 K. This high temperature region is not measured by most He TPD studies in the literature, whose absolute He content values are therefore too low. As the high temperature peak appears close to the temperature where the background, due to deuterium molecules, increases exponentially, the measurement of samples implanted with MeV He ions was postponed until the onset of the background has been pushed to higher temperatures by technical improvements to the setup. This decision was made as MeV implanted He must diffuse $\approx 1\,\mu m$ before it reaches the surface, while at 6 keV the distance is only $\approx 21\,nm$.

Instead of reducing the background by technical means, another possible path is to circumvent its effect. This could be achieved by using a high resolution QMS, that can distinguish between ^4He ($m = 4.003 amu$) and D_2 ($m = 4.028 amu$). Such a device is presently under procurement.

In future measurement campaigns the use of lower implantation fluences in combination with slower ramp rates should give the possibility to resolve desorption peaks representing specific detrapping energies. If this will not be achieved by adjusted experimental settings, another possible path to obtain specific values of detrapping energies and attempt frequencies will be the computational deconvolution of overlapping peaks measured in this work.

In summary, the results obtained using the new system are promising. They have shown how the setup can be further improved, while, despite the low number of measurements made, already providing an overview of the dynamics of the physical system, confirming some theoretical predictions.

Appendix A

Calculations

A.1 Relation for the Power Output of an Electron Beam Heater

In this section a derivation of the relation between heating filament current and sample temperature of the electron beam heater is given.

Equations

Radiative energy transport from surface 1 to 2:

$$\Phi_{1\to 2} = \epsilon_1\ \epsilon_2\ \sigma\left(T_1^4 - T_2^4\right) \qquad \left[\frac{\mathrm{W}}{\mathrm{m}^2}\right] \tag{A.1}$$

σ: Stefan-Boltzmann constant; ϵ_1, ϵ_2: emissivity of surface 1 and 2

Joule Heating:

$$P = I^2 R \qquad [\mathrm{W}] \tag{A.2}$$

I: current through the wire [A], *R: resistance of the wire* [Ω]

Richardson-Dushman equation [71] (Thermionic electron current):

$$i = C_0 T^2 \mathrm{e}^{-\frac{\phi}{kT}} \qquad \left[\frac{\mathrm{A}}{\mathrm{cm}^2}\right] \tag{A.3}$$

C_0: Richardson constant, ϕ: work function of the metal, k: Boltzmann constant

Approximation of the electrical resistance of a metal due to thermal phonons, valid at high temperatures [72]:

$$\rho_L \propto \frac{T}{M\theta_R^2} \tag{A.4}$$

M: atomic mass, θ_R: resistive characteristic temperature

Analysis of the System

The sample temperature in any equilibrium state is given by:

$$P_{in} = P_{out} \tag{A.5}$$

Neglecting any heating by photons from the filament, the only remaining energy source are electrons transferring their kinetic energy onto the sample. If bremsstrahlung as loss channel is neglected, it can be assumed that all kinetic electron energy is transferred to the sample:

$$P_{in} = U_{ac} I_{e^-} \tag{A.6a}$$

where U_{ac} is held constant by the power supply.

Secondly, the loss term can be assumed to be radiative only; therefore, equation A.1 holds.

$$P_{out} = A_s \epsilon_s \epsilon_{back} \sigma T_s^4 \tag{A.6b}$$

A_s: sample surface area, ϵ_s: emissivity of the sample; ϵ_{back}: emissivity of the vessel walls, T_s: sample temperature

Here it was assumed that $T_s \gg T_{background}$.

Inserting equation A.6a and A.6b in equation A.5 and rearranging gives:

$$T_s^4 = \frac{U_{ac}}{A_s \epsilon_s \epsilon_{back} \sigma} I_{e^-} \tag{A.7}$$

U_{ac} is held constant by the power supply of the electron beam heater, while A_s also is a known constant quantity and ϵ_s and ϵ_{back}, while in practice dependent on T_s, vary so little that they can be assumed to be constant and tabulated values can be used, therefore the only remaining unknown is I_{e^-}. It can be calculated from equation A.3:

$$I_{e^-} = A_{fil} C_0 T_{fil}^2 \mathrm{e}^{-\frac{\phi_{fil}}{kT_{fil}}} \tag{A.8}$$

T_{fil}: temperature of the filament, A_{fil}: surface area of the filament.

Therefore, the filament temperature needs to be calculated. This is done in the same manner as the sample temperature, the only difference being that the power source here is not an electron beam, but instead joule heating (equation A.2).

$$P_{in(joule)} = P_{out(radiative)} \tag{A.9}$$

$$I_{fil}^2 R_{fil} = A_{fil} \epsilon_{fil} \epsilon_{back} \sigma T_{fil}^4 \tag{A.10a}$$

I_{fil}: current through the electron providing filament, R_{fil} resistance of the filament, ϵ_{fil}: emissivity of the filament, T_{fil}: temperature of the filament.

Rearranging:

$$T_{fil}^4 = \frac{I_{fil}^2 R_{fil}}{A_{fil}\epsilon_{fil}\epsilon_{back}\sigma} \tag{A.10b}$$

Since R_{fil} is dependent on T_{fil}, it is approximated here by equation A.4.

$$T_{fil}^4 \propto \frac{I_{fil}^2 T_{fil}}{A_{fil}\epsilon_{fil}\sigma} \tag{A.10c}$$

$$T_{fil} \propto \left(\frac{I_{fil}^2}{A_{fil}\epsilon_{fil}\sigma}\right)^{\frac{1}{3}} \tag{A.10d}$$

Inserting equation A.10d in equation A.8 and then into equation A.7 gives the final relation:

$$T_s \propto \left(\frac{U_{ac}A_{fil}^{\frac{1}{3}}C_0}{A_s\epsilon_s}\frac{}{\epsilon_{fil}^{\frac{2}{3}}\sigma^{\frac{5}{3}}}\right)^{\frac{1}{4}} I_{fil}^{\frac{1}{3}} \mathrm{e}^{-\frac{\phi_{fil}}{\frac{4k}{(A_{fil}\epsilon_{fil}\sigma)^{\frac{1}{3}}} I_{fil}^{\frac{2}{3}}}} \tag{A.11a}$$

After reducing constants and fixed parameters:

$$T_s \propto C_1 I_{fil}^{\frac{1}{3}} \mathrm{e}^{-\frac{C_2}{I_{fil}^{\frac{2}{3}}}} \tag{A.11b}$$

List of Assumptions

There is no radiative heating of the sample.
The kinetic energy of the electrons is fully transferred to the sample.
The sample only uses energy via radiative transport.
The emissivities are temperature independent.

A.2 Pyrometer Reference Measurement

In order to confirm that the pyrometer measurement was accurate, a reference measurement was conducted by G. Holzner. A type C thermocouple was laser welded to a 15 mm diameter and 48 mm long tungsten cylinder. It was placed in a glass tube under vacuum. Then the cylinder was heated with a radio frequency induction furnace. The heating was controlled by a feedback loop with the type C thermocouple as input. A number of heat-hold-cooldown cycles was conducted. The pyrometer has a viewing angle perpendicular to the surface. The results, shown in figure A.1 be-

low, show excellent agreement between both measurements during the heating ramp. When set to hold a temperature of 2373 K, the measurements deviate by up to 80 K. During this hold time the temperature measured by the pyrometer slightly decreases together with the nominal power input. The deviation is, therefore, attributed to a change of the type C thermocouple.

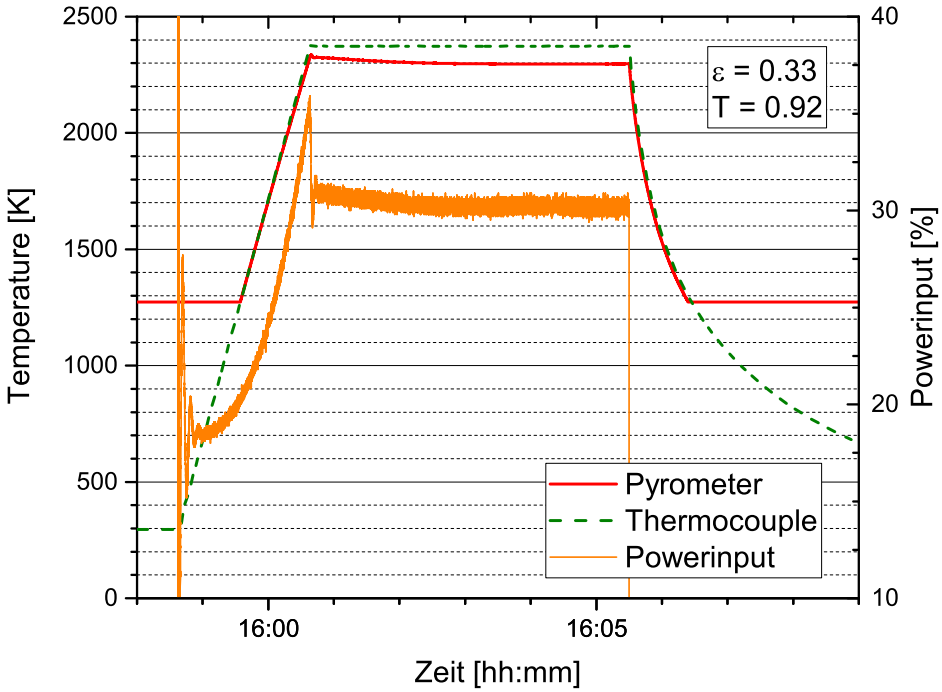

Figure A.1: The time evolution of nominal heating power and temperature as measured by pyrometer (red), thermocouple (green). The pyrometer settings were: $\epsilon = 0.33$ and a transmittance of UHV window of 0.92.

A.3 Depth Resolution of ERDA

The depth resolution of ERDA for the conditions of the setup used in this work is discussed in [9]. However, since this paper was published the physics model of SimNRA, the program used for the depth resolution calculation, has been improved. Therefore, figure 4 from the paper was recalculated with the most-up-to-date version of SimNRA, i.e., version 7.0.

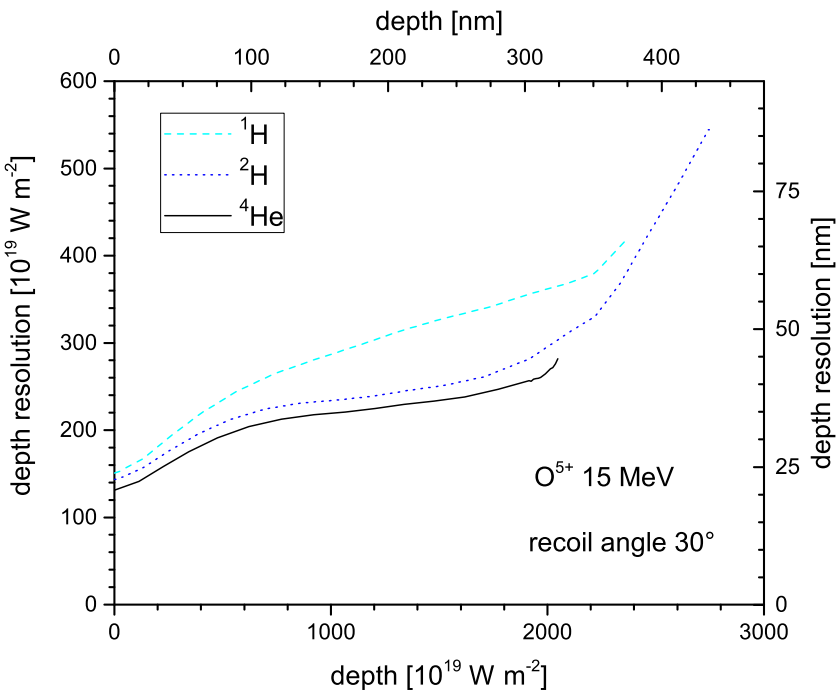

Figure A.2: Depth Resolution for the detection of ^{1}H, ^{2}H and ^{4}He in W with ERDA using 15 MeV O^{5+} at 30° recoil angle calculated with SimNRA 7.0.

While qualitatively there has been no change in calculated depth resolution, quantitatively it increased by approximately 25% near the surface and decreased by approximately the same amount for the remainder of the implantation depth.

A.4 Evaporation Rates

The temperatures reached in the setup are so high, that even the evaporation rates (Φ) of refractory metals such as Mo and W become relevant. Their evaporation rates are given in the figure below. The values are calculated from vapor pressure (p) values by equation:

$$\Phi = \frac{p}{\sqrt{2\ \pi\ M\ R\ T}} \tag{A.12}$$

Where M is the molar mass, R the universal gas constant and T the temperature.

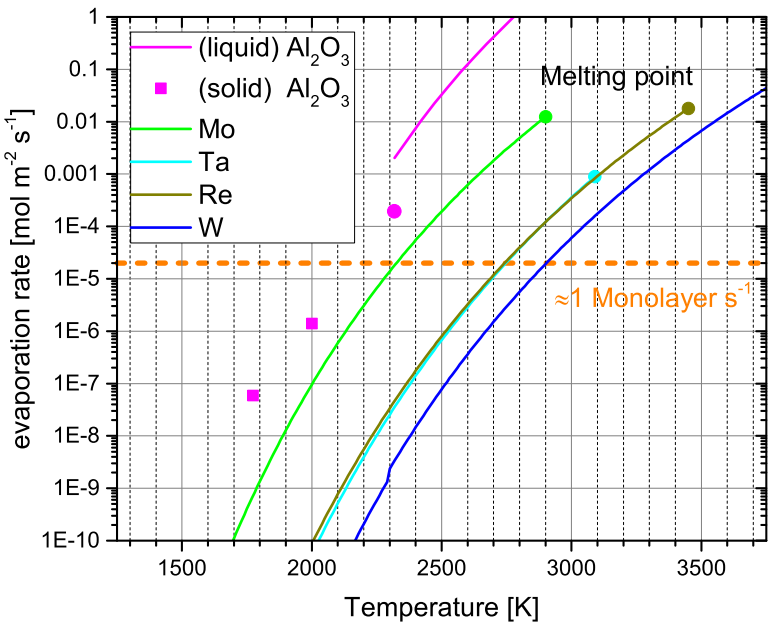

Figure A.3: The evaporation rates of selected materials with respect to temperature. Values for Mo,W,Ta obtained from [73] and Al_2O_3 from [74, 75] for the solid and [76] for the liquid phase

Appendix B

Tables

Sample number	Implantation device	Implantation energy and corresponding range [58]	Incident fluence [He m^{-2}]	Implantation flux [He $m^{-2}s^{-1}$]	ERDA	TPD ramp speed [K s^{-1}]
C0156	SIESTA	6 keV - 136 Å	1.86×10^{21}	2.1×10^{18}	-	2.3
C0158	SIESTA	6 keV - 136 Å	1.85×10^{21}	1.9×10^{18}	Y	1.0
C0165	SIESTA	6 keV - 136 Å	1.87×10^{21}	2.1×10^{18}	Y	-
C0166	PlaQ	100 eV - 7 Å	6.5×10^{20}	6.5×10^{17}	Y	-
C0168	PlaQ	100 eV - 7 Å	6.5×10^{19}	6.5×10^{17}	Y	-
C0169	SIESTA	6 keV - 136 Å	2.53×10^{21}	2.0×10^{18}	-	1.0
C0170	SIESTA	6 keV - 136 Å	1.85×10^{21}	1.9×10^{18}	-	1.0

Table B.1: Sample implantation conditions

Sample number	Implantation device	Implantation energy and corresponding range [58]	Incident fluence [He m^{-2}]	Implantation flux [He m^{-2} s^{-1}]
C0152	tandem	300 keV - 4998 Å	7.7×10^{20}	1.4×10^{15}
C0153	tandem	300 keV - 4998 Å	7.7×10^{20}	1.4×10^{15}
C0154	tandem	500 keV - 7591 Å	7.7×10^{20}	3×10^{15}
C0155	tandem	800 keV - 1.13×10^{4} Å	7.7×10^{20}	4.2×10^{15}
C0157	tandem	800 keV - 1.13×10^{4} Å	7.7×10^{19}	4.2×10^{15}
C0159	PlaQ	100 eV - 7 Å	6.5×10^{20}	6.5×10^{17}
C0160	tandem	800 keV - 1.13×10^{4} Å	7.7×10^{18}	4.2×10^{15}
C0162	SIESTA	6 keV - 136 Å	1.86×10^{20}	2.1×10^{18}
C0163	SIESTA	6 keV - 136 Å	1.86×10^{21}	1.9×10^{18}
C0164	PlaQ	100 eV - 7 Å	6.5×10^{19}	6.5×10^{17}
C0167	PlaQ	100 eV - 7 Å	6.5×10^{20}	6.5×10^{17}
C0171	PlaQ	100 eV - 7 Å	6.5×10^{19}	6.5×10^{17}

Table B.2: Sample implantation conditions for samples not measured

Name	Name in Code	value	units	source	ref.	comment
Implantation range of ion	rangeA	-	m	SRIM 2008.04	[58]	Implantation energy dependent
Straggling of ions	straggleA	-	m			
Fraction of reflected ions	reflA	-	-	Tabulated Data	[59]	
Layer thickness	layerthick	1, 0.3, 1, 100	µm	-	-	
Discretization of layers	layerdx	10, 10, 10, 10000	nm	-	-	
Activation Energy	filllevelEnergies	5.0, 3.1, 3.0, 2.9, 3.0, 2.6, 2.3	eV	DFT	[22] fig.6	Energy necessary for the escape of one He from trap filled with n He.
Attempt Frequency	filllevelFreq	2×10^{13}	s^{-1}	MD	[22]	Assumed to be the same for all trap levels.
		2×10^{15}			[18] p.48	

Trap density	trap level	3×10^{-4}, 3×10^{-3}, 1×10^{-5}, 1×10^{-5}	$\frac{trap}{W}$	SRIM calculation & measurement	[58]	Deduced from a combination of SRIM calculations and a measured depth profile of an 800 keV ^{3}He implanted sample. The depth profile was measured by D-NRA and deconvoluted in NRADC.
Migration Energy	EDiff	0.12	eV	ab initio	[60] fig.7	Values from 0.01 to 0.25 eV can be found in the literature.
Diffusion Coefficient	D0	2.5×10^{-8}	$\frac{\mathrm{m}^2}{\mathrm{s}}$			
Flux	fluxA	-	$\frac{\mathrm{He}}{\mathrm{m}^2\,\mathrm{s}}$	-	-	Particle flux - depends on the implantation device and its settings.

Table B.3: TESSIM-X input parameters

Bibliography

[1] D. Nishijima et al. »Micron-bubble formation on polycrystal tungsten due to low-energy and high-flux helium plasma exposure«. In: *Materials Transactions* 46.3 (2005), pp. 561–564. DOI: 10.2320/matertrans.46.561.

[2] Baldwin M.J. and Doerner R.P. »Helium induced nanoscopic morphology on tungsten under fusion relevant plasma conditions«. In: *Nuclear Fusion* 48.3 (2008), p. 035001. DOI: 10.1088/0029-5515/48/3/035001.

[3] Y. Gasparyan, V. Efimov and K. Bystrov. »Helium concentration measurement in tungsten fuzz-like nanostructures by means of thermal desorption spectroscopy«. In: *Nuclear Fusion* 56.5 (2016), p. 3. DOI: 10.1088/0029-5515/56/5/054002.

[4] P.A. Redhead. »Thermal desorption of gases«. In: *Vacuum* 12.4 (1962), pp. 203–211. DOI: 10.1016/0042-207X(62)90978-8.

[5] D. P. Corkhill and G. Carter. »Radiation enhanced diffusion of trapped inert gases in tungsten«. In: *Nuclear Instruments and Methods* 38.DEC (1965), 192pp. DOI: 10.1016/0029-554x(65)90135-7.

[6] E. V. Kornelsen. »Entrapment of Helium Ions at (100) and (110) Tungsten Surfaces«. In: *Canadian Journal of Physics* 48.23 (1970), pp. 2812–+.

[7] E. V. Kornelsen. »The interaction of injected helium with lattice defects in a tungsten crystal«. In: *Radiation Effects* 13.3-4 (1972), pp. 227–236. DOI: 10.1080/00337577208231184.

[8] A. A. van Gorkum and E. V. Kornelsen. »The Entrance Probability and Range of Helium in W(100) for Energies 8 eV to 5000 eV as measured by thermal-desorbtion spectrometry«. In: *Radiation Effects and Defects in Solids* 52.1-2 (1980), pp. 25–33. DOI: 10.1080/00337578008210013.

[9] E. Markina, M. Mayer and H. T. Lee. »Measurement of He and H depth profiles in tungsten using ERDA with medium heavy ion beams«. In: *Nuclear Instruments and Methods in Physics Research Section B* 269.24 (2011), pp. 3094–3097. DOI: 10.1016/j.nimb.2011.04.075.

[10] J. H. You et al. »European DEMO divertor target: Operational requirements and material-design interface«. In: *Nuclear Materials and Energy* 9 (2016), pp. 171–176. DOI: 10.1016/j.nme.2016.02.005.

[11] N. Yoshida. »Review of recent works in development and evaluation of high-Z plasma facing materials«. In: *Journal of Nuclear Materials* 266 (1999), pp. 197–206. DOI: 10.1016/s0022-3115(98)00817-4.

[12] R. P. Doerner et al. »Quantitatively measuring the influence of helium in plasma-exposed tungsten«. In: *Nuclear Materials and Energy* (2016). DOI: 10.1016/j.nme.2016.09.002.

[13] M. Shimada and B. J. Merrill. »Tritium decay helium-3 effects in tungsten«. In: *Nuclear Materials and Energy* (2016). DOI: 10.1016/j.nme.2016.11.006.

[14] N. Yoshida et al. »Impact of low energy helium irradiation on plasma facing metals«. In: *Journal of Nuclear Materials* 337.1-3 (2005), pp. 946–950. DOI: 10.1016/j.jnucmat.2004.10.162.

[15] K. Tokunaga et al. »Synergistic effects of high heat loading and helium irradiation of tungsten«. In: *Journal of Nuclear Materials* 329 (2004), pp. 757–760. DOI: 10.1016/j.jnucmat.2004.04.178.

[16] Charles Kittel. *Introduction to solid state physics*. 5.ed. New York: Wiley, 1976, p. 542. ISBN: 0-471-49024-5.

[17] A Manhard. »Deuterium Inventory in Tungsten after Plasma Exposure: A Microstructural Survery«. Thesis. Universität Augsburg, 2012. URL: http://hdl.handle.net/11858/00-001M-0000-0026-E65E-6.

[18] A. van Veen. »Helium Defect Interactions in Metals and Silicon«. In: *Fundamental Aspects of inert Gases in Solids*. Ed. by S.E. Donnelly and J.H. Evans. New York: Plenum Press, 1991.

[19] C. Kittel. *Introduction to solid state physics*. 8th. Wiley, 2005, 587pp. ISBN: 0-471-49024-5.

[20] W.D. Wilson and R.A. Johnson. »Rare Gases in Metals«. In: *Interatomic Potentials and Simulation of Lattice Defects*. Ed. by Pierre C. Gehlen, Joe R. Beeler and Robert I. Jaffee. Boston, MA: Springer US, 1972, p. 383. ISBN: 978-1-4684-1992-4. DOI: 10.1007/978-1-4684-1992-4.

[21] M. S. Abd El Keriem, D. P. van der Werf and F. Pleiter. »Helium-vacancy interaction in tungsten«. In: *Physical Review B* 47.22 (1993), pp. 14771–14777. DOI: 10.1103/PhysRevB.47.14771.

[22] J. Boisse et al. »Modeling of the self trapping of helium and the trap mutation in tungsten using DFT and empirical potentials based on DFT«. In: *Journal of Materials Research* 29.20 (2014), pp. 2374–2386. DOI: 10.1557/jmr.2014.258.

[23] K. O. E. Henriksson, K. Nordlund and J. Keinonen. »Molecular dynamics simulations of helium cluster formation in tungsten«. In: *Nuclear Instruments and Methods in Physics Research Section B* 244.2 (2006), pp. 377–391. DOI: 10.1016/j.nimb.2005.10.020.

[24] E. V. Kornelsen and A. A. van Gorkum. »A study of Bubble Nucleation in Tungsten using Thermal-Desorption Spectrometry: Clusters of 2 to 100 Helium Atoms«. In: *Journal of Nuclear Materials* 92.1 (1980), pp. 79–88. DOI: 10.1016/0022-3115(80)90144-0.

[25] A. A. van Gorkum and E. V. Kornelsen. »Quantitative thermal desorption spectrometry of ionically implanted inert gases—I. Fundamental aspects«. In: *Vacuum* 31.2 (1981), pp. 89–98. DOI: 10.1016/S0042-207X(81)80165-0.

[26] E. V. Kornelsen and A. A. van Gorkum. »Quantitave thermal desorption spectrometry of ionically implanted inert gases—II. Technical requirements«. In: *Vacuum* 31.2 (1981), pp. 99–111. DOI: 10.1016/s0042-207x(81)80166-2.

[27] J. Guterl et al. »Theoretical analysis of deuterium retention in tungsten plasma-facing components induced by various traps via thermal desorption spectroscopy«. In: *Nuclear Fusion* 55.9 (2015), p. 093017. DOI: 10.1088/0029-5515/55/9/093017.

[28] C. Kittel. *Introduction to solid state physics*. 8th. Wiley, 2005, p. 112. ISBN: 0-471-49024-5.

[29] P. Alnot, A. Cassuto and D. A. King. »Adsorption and Desorption-Kinetics with no Precursor Trapping - Hydrogen and Deuterium on W(100)«. In: *Surface Science* 215.1-2 (1989), pp. 29–46. DOI: 10.1016/0039-6028(89)90697-3.

[30] J. Bauer. »Hydrogen Isotope Exchange in Tungsten at low Temperatures«. Thesis. Technische Universität München, 2017.

[31] K. Schmid, U. von Toussaint and T. Schwarz-Selinger. »Transport of hydrogen in metals with occupancy dependent trap energies«. In: *Journal of Applied Physics* 116.13 (2014), p. 11. DOI: 10.1063/1.4896580.

[32] Wolfram Research Inc. *Mathematica*. Version 10.4. Champaign, Illinois: Wolfram Research, Inc., 2016.

[33] K. Schmid et al. »Recent Progress in the Understanding of H Transport and Trapping in W«. In: *Physica Scripta* T170 (2017). accepted.

[34] B. Wielunska et al. »Cross section data for the D(He-3,p)He-4 nuclear reaction from 0.25 to 6 MeV«. In: *Nuclear Instruments and Methods in Physics Research Section B* 371 (2016), pp. 41–45. DOI: 10.1016/j.nimb.2015.09.049.

[35] P. Wang et al. »Comparing deuterium retention in tungsten films measured by temperature programmed desorption and nuclear reaction analysis«. In: *Nuclear Instruments and Methods in Physics Research Section B* 300 (2013), pp. 54–61. DOI: 10.1016/j.nimb.2013.01.057.

[36] A. Manhard, G. Matern and M. Balden. »A Step-By-Step Analysis of the Polishing Process for Tungsten Specimens«. In: *Praktische Metallographie-Practical Metallography* 50.1 (2013), pp. 5–16.

[37] A. Manhard, M. Balden and S. Elgeti. »Quantitative Microstructure and Defect Density Analysis of Polycrystalline Tungsten Reference Samples after Different Heat Treatments«. In: *Praktische Metallographie-Practical Metallography* 52.8 (2015), pp. 437–466. DOI: 10.3139/147.110354.

[38] A. Manhard, T. Schwarz-Selinger and W. Jacob. »Quantification of the deuterium ion fluxes from a plasma source«. In: *Plasma Sources Science and Technology* 20.1 (2011), p. 9. DOI: 10.1088/0963-0252/20/1/015010.

[39] F. M. Bacon, R. W. Bickes and J. B. Ohagan. »Gas-Discharge Ion-Source. II. Duopigatron«. In: *Review of Scientific Instruments* 49.4 (1978), pp. 435–439. DOI: 10.1063/1.1135444.

[40] W. Eckstein et al. *Sputtering Data*. Report. Max-Planck-Institut für, Plasmaphysik, 1993. URL: http://hdl.handle.net/11858/00-001M-0000-0027-6324-6.

[41] R. Arredondo Parra. The article will be published in "Nuclear Instruments and Methods in Physics Research Section B" or in "Review of Scientific Instruments". unpublished.

[42] T. Schwarz-Selinger. »Deuterium retention in MeV self-implanted tungsten: Influence of damaging dose rate«. In: *Nuclear Materials and Energy* (2017). DOI: https://doi.org/10.1016/j.nme.2017.02.003.

[43] F. J. Norton. »Helium Diffusion through Glass«. In: *Journal of the American Ceramic Society* 36.3 (1953), pp. 90–96. DOI: 10.1111/j.1151-2916.1953.tb12843.x.

[44] K. Saha. *The Earth's Atmosphere - Its Physics and Dynamics*. Spinger, 2008, p. 367. ISBN: 978-3-540-78427-2. DOI: 10.1007/978-3-540-78427-2.

[45] I. S. Lupakov and Yu.S. Kuzmichev. »An Investigation of Permeability of Metal Pipe Walls with respect to Helium«. In: *Journal of Nuclear Energy Parts a and B-Reactor Science and Technology* 19.6 (1965), pp. 484–489. DOI: 10.1016/0368-3230(65)90057-1.

[46] A. A. Rusinov et al. »A setup for thermodesorption measurements«. In: *Instruments and Experimental Techniques* 52.6 (2009), pp. 871–876. DOI: 10.1134/s0020441209060219.

[47] J. Pierre and D. Paulmier. »Capture et réémission de l'hélium par le tungstène polycristallin soumis à un bombardement ionique«. In: *Comptes Rendus Hebdomadaires Des Seances De L Academie Des Sciences Serie B* 280.9 (1975), pp. 275–278.

[48] Yu. Gasparyan et al. *Investigation of H and He interaction with radiation defects in tungsten by means of thermal desorption spectroscopy.* talk at 3rd International Workshop on Models and Data for Plasma-Material Interaction in Fusion Devices (MoD-PMI 2017). conference talk. Jülich, Germany, May 2017.

[49] R Seiwert. »Die Elektronenhülle des Atoms«. In: *Aufbau der Materie.* Ed. by H.Gobrecht. 2nd ed. Vol. 4. Bergmann-Schaefer Lehrbuch der Experimentalphysik. Berlin: Walter de Gruyter, 1981. Chap. II, p. 168.

[50] H. Lüth. *Solid Surfaces, Interfaces and Thin Films.* 6th. Graduate Texts in Physics. Springer, 2015, 559pp. DOI: 10.1007/978-3-319-10756-1.

[51] Igor L. Shabalin. *Ultra-High Temperature Materials I: Carbon (Graphene/Graphite) and Refractory Metals.* Vol. 1. Netherlands: Springer, 2014, p. 794. DOI: 10.1007/978-94-007-7587-9.

[52] G. Holzner. »private communication«. 2017.

[53] L. K. Thomas. »Thermal Radiation from rough Tungsten Surfaces in normal and off-normal Directions«. In: *Journal of Applied Physics* 39.10 (1968), p. 4681. DOI: 10.1063/1.1655819.

[54] I. Langmuir. »The electron emission from thoriated tungsten filaments«. In: *Physical Review* 22.4 (1923), pp. 0357–0398. DOI: 10.1103/PhysRev.22.357.

[55] D. A. Dahl, J. E. Delmore and A. D. Appelhans. »SIMION PC/PS2 electrostatic Lens Design Program«. In: *Review of Scientific Instruments* 61.1 (1990), pp. 607–609. DOI: 10.1063/1.1141932.

[56] T. Kalvas et al. »IBSIMU: A three-dimensional simulation software for charged particle optics«. In: *Review of Scientific Instruments* 81.2 (2010), p. 3. DOI: 10.1063/1.3258608.

[57] S. B. Gilliam et al. »Helium retention and surface blistering characteristics of tungsten with regard to first wall conditions in an inertial fusion energy reactor«. In: *Nuclear Instruments and Methods in Physics Research Section B* 241.1-4 (2005), pp. 491–495. DOI: 10.1016/j.nimb.2005.07.060.

[58] J. F. Ziegler. »SRIM-2003«. In: *Nuclear Instruments and Methods in Physics Research Section B* 219 (2004), pp. 1027–1036. DOI: 10.1016/j.nimb.2004.01.208.

[59] W. Eckstein. *Reflection (Backscattering)*. Report. Max-Planck-Institut für, Plasmaphysik, 2009. URL: http://hdl.handle.net/11858/00-001M-0000-0026-F340-E.

[60] J. Wang et al. »Atomistic simulations of helium behavior in tungsten crystals«. In: *Journal of Nuclear Materials* 427.1-3 (2012), pp. 290–296. DOI: 10.1016/j.jnucmat.2012.05.020.

[61] K. O. E. Henriksson, K. Nordlund and J. Keinonen. »Molecular dynamics simulations of helium cluster formation in tungsten«. In: *Nuclear Instruments and Methods in Physics Research Section B* 244.2 (2006), pp. 377–391. DOI: 10.1016/j.nimb.2005.10.020.

[62] M. Mayer. *SIMNRA user's guide*. Report 9/113. IPP, 1997. URL: http://hdl.handle.net/11858/00-001M-0000-0027-6157-F.

[63] A. F. Gurbich. »Evaluated differential cross-sections for IBA«. In: *Nuclear Instruments and Methods in Physics Research Section B* 268.11-12 (2010), pp. 1703–1710. DOI: 10.1016/j.nimb.2010.02.011.

[64] J. Demarche and G. Terwagne. »Precise measurement of the differential cross section from the 16-O(alpha,alpha)16-O elastic reaction at 165 degrees and 170 degrees between 2.4 and 6.0 MeV«. In: *Journal of Applied Physics* 100.12 (2006). DOI: 10.1063/1.2402868.

[65] J. Skilling. »Calibration and interpolation«. In: *26th International Workshop on Bayesian Inference and Maximum Entropy Methods in Science and Engineering*. Vol. 872. Aip Conference Proceedings. MELVILLE: Amer. Inst. Physics, 2006, pp. 321–330. ISBN: 978-0-7354-0371-0.

[66] M. Guitart Corominas and T. Schwarz-Selinger. In: *Nuclear Instruments and Methods in Physics Research Section B* (2017). submitted.

[67] J. Pierre and D. Paulmier. »Influence des défauts créés par un bombardement primaire sur la fixation de l'hélium dans le tungsténe«. In: *Comptes Rendus Hebdomadaires Des Seances De L Academie Des Sciences Serie B* 281.16 (1975), pp. 353–356.

[68] H. T. Lee et al. »Incident Ion Energy and Temperature Dependence of Helium Bubble Formation and Its Impact on D-Retention under Simultaneous He-D Irradiation of Tungsten«. In: *Fusion Science and Technology* 63.1T (2013), pp. 233–236. DOI: 10.13182/FST13-A16913.

[69] K. Schmid et al. »The implications of high-Z first-wall materials on noble gas wall recycling«. In: *Nuclear Fusion* 47.8 (2007), pp. 984–989. DOI: 10.1088/0029-5515/47/8/032.

[70] G. Terwagne et al. »Cross-section measurements of the ^{14}N(α,p)^{17}O and ^{14}N(α,α)^{14}N reactions between 3.5 and 6 MeV«. In: *Journal of Applied Physics* 104.8 (2008), p. 8. DOI: 10.1063/1.3000661.

[71] Erik Lassner. *Tungsten Properties, Chemistry, Technology of the Element, Alloys, and Chemical Compounds*. Boston, MA: Springer US, 1999, p. 40. ISBN: 9781461549079. DOI: 10.1007/978-1-4615-4907-9.

[72] Charles Kittel. *Introduction to solid state physics*. 5.ed. New York: Wiley, 1976, p. 172. ISBN: 0-471-49024-5.

[73] Online Database. 2016. URL: https://www.iap.tuwien.ac.at/www/surface/vapor_pressure.

[74] Richard P. Burns. »Systematics of the Evaporation Coefficient Al2O3, Ga2O3, In2O3«. In: *The Journal of Chemical Physics* 44.9 (1966), pp. 3307–3319. DOI: 10.1063/1.1727229.

[75] A. Nara and H. Satoh. »Sputtering Target and Process for Manufacturing Same Search«. Patent WO/2013/145818 (Japan). JX NIPPON MINING and METALS CORPORATION. 2013. URL: https://patentscope.wipo.int/search/en/detail.jsf?docId=WO2013145818 (visited on 29/09/2017).

[76] Carl L. Yaws and Marco A. Satyro. »Chapter 2 - Vapor Pressure – Inorganic Compounds«. In: *The Yaws Handbook of Vapor Pressure (Second Edition)*. Gulf Professional Publishing, 2015, pp. 315–322. ISBN: 978-0-12-802999-2. DOI: https://doi.org/10.1016/B978-0-12-802999-2.00002-7.

List of Figures

2.1 IBA Setup Layout 13
2.2 Radial Flux Distribution of the low-temperature Plasma Source . . . 15

3.1 Vertical cut through TESS 21
3.2 Photographs of the Sample Holder and Electron Source 23
3.3 Sample Holder and Electron Beam Source Drawing and 3-D Redering 24
3.4 Sample Heating Curve 26
3.5 Electron Beam Heater Simulation 28
3.6 Experimental Pumping Time Constant Determination 29
3.7 Cold Trap Activation 29
3.8 Particle Flux Background in TESS 30

4.1 TESSIM-X - Attempt Frequency Variation 35
4.2 TESSIM-X - Fluence Variation 36
4.3 TESSIM-X - Implantation Energy Variation 37
4.4 ERDA of a-C:H:D:He Layer (Calibration) 39
4.5 NRA of a-C:H:D:He Layer (Calibration) 41
4.6 ERDA of He-implanted W Samples 42
4.7 He Depth Profiles from ERDA 43
4.8 SRIM - He Implantation Depth Profile 44
4.9 TPD Measurements - Effusion Flux vs. Time 46
4.10 TPD Measurements - Effusion flux vs temperature 49
4.11 TPD - Heating Ramp Rate Variation 51
4.12 TPD - Heating Ramp Rate Variation - Detailed 52
4.13 TPD - Effect of Ion Beam Damage 53
4.14 TPD - Effect of Ion Beam Damage on low-temperature Peak 54
4.15 TPD - Desorption Peak Ratios 55
4.16 He Retention Plot from TPD and ERDA 57
4.17 Comparison of TESSIM-X and Experimental Results 58

A.1 Pyrometer Reference Measurement 66
A.2 Depth Resolution of ERDA 67
A.3 Evaporation Rates 68

List of Tables

4.1 TESSIM-X - Input Parameters 34
4.2 TESSIM-X - Implantation Energy Dependent Parameters 35

B.1 Sample Implantation Conditions 70
B.2 Sample Implantation Conditions for Samples not Measured 71
B.3 TESSIM-X - Input Parameters (detailed) 73

Acknowledgments

Folgenden Personen bin ich zum Dank verpflichtet:

Herrn Prof. Neu dafür, dass er die Arbeit betreut und mir den Besuch der PFMC ermöglicht hat.

P. Feulner für die Zweitbegutachtung der Arbeit.

W. Jacob, für die Chance, in der PMI-Forschungsgruppe mitarbeiten zu dürfen und auch besonders für die sehr gründlich Korrektur der Arbeit.

Thomas S. für die Exzellente Betreuung in allen Belangen.

Thomas D. für seine Unterstüzung beim Umbau von TESS und für die Beantwortung aller meiner Fragen zum Themenbereich Vakuumsysteme.

Georg ebenfalls für die Beratung und praktische Hilfe beim Umbau von TESS.

Der E2M Bereichswerkstatt - hier insbesondere Herrn Hoffmann - für die Fertigung der TZM und Mo Teile.

Herrn Eismann für die Diskussionen zum Thema Wolframbearbeitung und seinem Team von der ASDEX Werkstatt für die fertigung aller Wolframkomponenten des Versuchsaufbaus.

Arne für alle Elektroinstallationsarbeiten an TESS

Armin für die He implantationen an PlaQ.

Rodrigo für die in SIESTA implantierten Proben.

Den Operatoren des Tandembeschleunigers für die viele Implantationszeit.

Arno für die Einführung in die Nutzung des CAD-Programms Inventor.

Michi für vieles - unter anderem - für die Tandemimplantationen und für kurzfristige Hilfe beim (Ein-)bau des Electronenstrahlheizers.

Klaus für die Rechnungen in IBSIMU und für die Bereitstellung von, und Hilfe mit TESSIMX.

Johannes für die Unterstützung bei der Benutzung von TESSIM-X.

Matej für die Beantwortung vieler Fragen zur Benutzung von SimNRA und zu IBA generell.

Laurence für die Hilfe beim Verstehen der beiden nur auf französisch vorhandenen Fachartikel.

meinem Vater, der nicht aufgehört hat, mich daran zu erinnern, dass ich doch eigentlich eine Röntgenquelle baue.

meiner Mutter, stellvertretend für alle SteuerzahlerInnen, für das mir zu Verfügung gestellte Budget.

Leo für den letzten Korrekturdurchgang.